CHARA Interferometry and *TESS* Asteroseismology of the Core-Helium Burning Red Giant κ Cyg

Arnab Chowhan[1★], Timothy R. Bedding[1], Daniel Huber[2], J. M. Joel Ong(王加冕)[1], Lea S. Schimak[1], Yaguang Li(李亚光)[2], Courtney L. Crawford[1], Timothy R. White[1]
[1]*Sydney Institute for Astronomy, School of Physics, University of Sydney, Sydney, NSW 2006, Australia*
[2]*Institute for Astronomy, University of Hawai'i, 2680 Woodlawn Drive, Honolulu, HI 96822, USA*

Accepted XXX. Received YYY; in original form ZZZ

ABSTRACT

We present a detailed study of the secondary red clump star, κ Cyg, by combining long-baseline visible interferometry using the PAVO beam combiner at the CHARA Array with high-precision asteroseismology from *TESS*. This dual approach allowed for a stringent test of stellar evolutionary models in the core helium-burning phase, which remains a regime of significant theoretical uncertainty. Using the PAVO interferometric data and fitting the limb-darkened intensity profile directly, we measured $R = 8.65 \pm 0.10$ R$_\odot$. We fitted the spectral energy distribution (SED) using Phoenix model atmospheres and calculated $L = 44.46 \pm 1.09$ L$_\odot$ and $T_{\rm eff} = 5066^{+47}_{-50}$ K. Using 16 sectors of *TESS* photometry, we detected clear solar-like oscillations in κ Cyg. Through comparison of oscillation frequencies with MESA grids using either predictive mixing (PM) or exponential overshooting (OS), we found that models reproducing the oscillation frequencies systematically overestimate the stellar radius, with overshooting models performing only marginally better. The same models also under-predict the observed dipole-mode period spacing ($\Delta\Pi_1$). By inspecting the phase offset (ϵ_p), we conclude that models misrepresent the interior structure of the star. Our results demonstrate that matching envelope-dominated asteroseismic observables alone is insufficient to ensure a correct core or even global structure, and highlight the need for improved treatments of convective boundary mixing in the models of core helium-burning (CHeB) stars.

Key words: asteroseismology – stars: fundamental parameters – stars: horizontal branch – stars: oscillations – techniques: interferometric

1 INTRODUCTION

Asteroseismology and long-baseline interferometry are, separately, already powerful observational techniques. Combined, they have the potential ability to determine fundamental stellar properties with a level of precision that neither technique can achieve in isolation. This synergy provides a powerful framework for testing stellar models by linking probes of stellar interiors with independent constraints on stellar size and effective temperature.

Over the past two decades, space-based photometry from *CoRoT*, *Kepler* and *TESS* (e.g., Chaplin & Miglio 2013; Hekker & Christensen-Dalsgaard 2017; García & Ballot 2019; Jackiewicz 2021; Aerts 2021; Huber 2025), complemented by ground-based radial velocities (e.g., Campante et al. 2024; Lundkvist et al. 2024; Li et al. 2025), has turned asteroseismology into a mature observational discipline, delivering precise masses, radii, and evolutionary states for thousands of stars. Yet precision alone is not sufficient: the radii and masses inferred from asteroseismic modelling are only as reliable as the physical assumptions built into the stellar evolution models themselves. Asteroseismic radius, rather than being a direct measurement of a star's physical size, corresponds to the radius of the stellar model whose computed mode frequencies best reproduce the observed oscillation spectrum. Therefore, it is sensitive to the adopted prescriptions for interior physics, chemical mixing, and the treatment of near-surface layers.

This model-dependence is most acute for stars undergoing core helium burning (CHeB). Once a star exhausts hydrogen in its core and ignites helium, it develops strong chemical gradients at multiple locations in its interior, governed by convective boundary mixing, one of the most uncertain processes in stellar physics. Secondary red clump stars, which are intermediate-mass stars burning helium in a non-degenerate core, are valuable targets for testing these prescriptions. They occupy a narrow region of the Hertzsprung–Russell diagram, overlapping with both primary red clump stars and ascending red giant branch stars (Girardi 1999, 2016), making them difficult to identify photometrically. Despite their potential, CHeB stars have received comparatively little focused asteroseismic attention (e.g., De Moura et al. 2020; Murphy et al. 2021; Brogaard et al. 2023), with most modelling efforts concentrated on reproducing their global properties rather than their individual mode frequencies (e.g., Bossini et al. 2015, 2017; Constantino et al. 2015; Noll & Deheuvels 2023; Noll et al. 2025).

An independent and complementary measurement of stellar properties is provided by long-baseline interferometry. Unlike asteroseismology, interferometry determines angular diameters directly from the spatial coherence of the stellar disk, yielding radii that are largely

★ E-mail: acho0151@uni.sydney.edu.au

independent of assumptions about interior physics (e.g., Quirrenbach et al. 1996). However, a weak model-dependence does enter through the limb-darkening coefficients required to convert the observed stellar visibility into an angular diameter. By sampling interferometric measurements beyond the first stellar visibility null, where the visibility curve is most sensitive to the intensity profile of the stellar disk, one can reduce reliance on hydrodynamic atmosphere models and even use the data to test the models directly (e.g., Kervella et al. 2017).

Combined with precise parallaxes from *Gaia* (Gaia Collaboration 2022) and bolometric fluxes (e.g., Boyajian et al. 2014), interferometry delivers direct measurements of stellar radii and effective temperatures. The complementarity of the two techniques has been well established across the H–R diagram (e.g., North et al. 2007; Mazumdar et al. 2009; Huber et al. 2012; White et al. 2013; Johnson et al. 2014; Hjørringgaard et al. 2017; Stokholm et al. 2019; Li et al. 2025). This makes interferometry not merely a tool for improving parameter precision, but a genuine test of stellar structure theory, one that we exploit here for the first time in a secondary red clump star.

In this work, we present the first combined analysis of interferometric observations and detailed asteroseismic modelling of individual oscillation modes for a secondary red clump star. By using interferometric measurements beyond the first visibility null, we directly test hydrodynamic atmosphere models and the limb-darkening coefficients they predict. We then compare the resulting stellar radii and effective temperatures against asteroseismic model predictions to investigate how well current stellar models, with their prescribed treatments of convective boundary mixing and near-surface layers, reproduce the internal and external structure of a core helium burning star, with implications for our understanding of mixing in evolved stars.

2 PROPERTIES OF κ CYG

We target the bright G8 red giant κ Cyg (HR 7328; HD 181276; HIP 94779) for several practical and scientific reasons. It is a nearby evolved star (parallax ϖ_{Gaia} = 26.49 mas) whose brightness (V = 3.76) makes it an excellent target for long-baseline interferometric observations. At the same time, it is not bright enough to saturate the *TESS* detectors and produce long bleeding columns in the target pixel files (TPFs), which would require special techniques to extract high-quality photometry (Rudrasingam et al. 2026). The resulting asteroseismic data allow a clear identification of its evolutionary state using established diagnostics based on dipolar mixed modes (e.g. Bedding et al. 2011; Mosser et al. 2012). As a secondary clump star, κ Cyg therefore provides a rare opportunity to obtain both interferometric and asteroseismic constraints on a star in this evolutionary phase.

Numerous spectroscopic studies have analysed κ Cyg and provide well-constrained atmospheric parameters. We adopted the effective temperature, $T_{\rm eff}$ = 5021 ± 100 K, surface gravity, $\log g$ = 3.02 ± 0.08 and metallicity, [Fe/H] = 0.10 ± 0.07 from Deka-Szymankiewicz et al. (2018), with uncertainties chosen to be conservative and consistent with typical spectroscopic analyses (Bruntt et al. 2010; Tayar et al. 2022). These parameters are used in section 3.2 to compute the limb-darkened angular diameter ($\theta_{\rm LD}$) using 3D STAGGER atmosphere models.

κ Cyg has previously been studied using NPOI (Navy Prototype Optical Interferometer; Benson et al. 2003) and its interferometric $\theta_{\rm LD}$ was measured to be 2.143 ± 0.008 mas (Baines et al. 2018). In the present work, we employ new visible-wavelength interferometric observations from the PAVO beam combiner at the CHARA Array, with visibility measurements extending well beyond the first null, allowing a more robust and less model-dependent determination of the stellar intensity profile.

The *Gaia* DR3 solution for κ Cyg yields a RUWE (re-normalised unit weight error) of 2.29, which indicates excess astrometric noise that is usually ascribed to binarity (Castro-Ginard et al. 2024). However, no evidence for binarity has been reported in the literature, and no signatures of a companion are detected in the asteroseismic power spectrum. We therefore treat κ Cyg as a single star in the analysis that follows.

We did not employ any Doppler correction to our power spectrum since the radial velocity of κ Cyg is 29.36 ± 0.03 km s^{-1} (Deka-Szymankiewicz et al. 2018), corresponding to a frequency shift of $\sim$ 0.01 μHz, which is well below the observational uncertainties in the frequency range of interest.

3 INTERFEROMETRY

3.1 Observations

We obtained interferometric observations using the Precision Astronomical Visible Observations (PAVO) beam combiner at the Center for High Angular Resolution Astronomy (CHARA) Array (ten Brummelaar et al. 2005) at Mount Wilson Observatory, California. PAVO is a pupil-plane beam combiner operating mainly in the visible spectrum (630–900 nm), spectrally dispersing light across several independent channels. The CHARA Array provides 15 possible baselines, with the longest being the S1E1 telescope configuration (330 m). Operating at visible wavelengths grants PAVO high spatial resolution and it has a limiting magnitude of approximately $R \sim$ 7–8, depending on seeing conditions. A detailed description of the instrument can be found in Ireland et al. (2008).

We used PAVO in two-telescope mode over seven nights between 2018 April and 2020 July. Observations were performed using the W1W2 (107.93 m) and E1E2 (65.88 m) baselines, selected to sample both within and beyond the first null of the stellar visibility function. The complete log of our observations, including dates, telescope configurations and calibrators, is provided in Table 1. The corresponding coverage in the spatial frequency plane is illustrated in Fig. 1. The points are colour-coded by wavelength channel, demonstrating the broad (u, v) coverage from only two baselines.

For each scan, we observed calibrators immediately before and after observing our target to track the interferometric transfer function. A bright, unresolved point source close to the target object is ideal for calibration to ensure spatially and temporally similar observations. We selected B stars as calibrators since these are intrinsically bright and distant enough to have angular diameters ($\leq$ 0.2 mas) too small to be resolved by PAVO. The full list of calibrators is provided in Table 2. We also observed ι^1 Cyg (HD 183534) but excluded it from the list of calibrators since its raw visibilities showed structure indicative of a probable companion.

The expected angular sizes of the calibrators (θ_{V-K}) were calculated using the empirical $V - K$ surface-brightness relation from Boyajian et al. (2014). We took V magnitudes from the Tycho catalogue (Ammons et al. 2006) and converted to the Johnson system following Bessell (2000), while K magnitudes were taken from the Two Micron All Sky Survey (2MASS; Skrutskie et al. 2006). We estimated the interstellar reddening for each calibrator using the 3D dust maps from Green et al. (2019) and followed the extinction law from O'Donnell (1994) to deredden the magnitudes.

UT Date	No. of Observations	Telescopes	Baseline	Calibrator Stars
2018 April 22	4	W1W2	107.93	HD 177003, HD 188252
2018 April 23	4	W1W2	107.93	HD 177003, HD 188252
2018 June 02	4	W1W2	107.93	HD 177003, HD 188252
2018 August 05	4	E1E2	65.88	HD 177003, HD 188252, HD 175640
2019 August 24	4	E1E2	65.88	HD 177003
2019 August 25	2	W1W2	107.93	HD 177003
2020 July 22	4	E1E2	65.88	HD 177003, HD 188252

Table 1. Log of interferometric observations for κ Cyg.

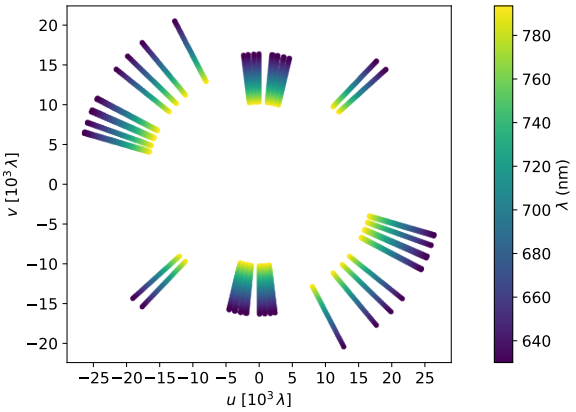

Figure 1. Spatial frequency coverage of κ Cyg with 7 nights of PAVO observations in two-telescope mode. The points are colour-coded by wavelength, with bluer corresponding to lower wavelengths, shown in the colour map on the right.

HD	Sp. T.	$V-K$	E_{B-V}	θ_{V-K} (mas)
177003	B2.5IV	-0.518	0.000	0.209
188252	B2III	-2.807	0.090	0.047
175640	B9III	-4.095	0.871	0.055

Table 2. Calibrators observed by PAVO for κ Cyg and their properties.

We have used the 28 central wavelength channels for our analysis and employed the PAVO data-reduction pipeline, which has been used for numerous two-telescope visibility studies (e.g., Bazot et al. 2011; Derekas et al. 2011; Huber et al. 2012; White et al. 2013; Maestro et al. 2013). The calibrated squared-visibility measurements for κ Cyg as a function of spatial frequency are presented in Fig. 2. The data points, from a total of 26 scans, are colour-coded by wavelength channel, consistent with Fig. 1.

3.2 Visibility Modelling

We illustrate the need to account for the centre-to-limb intensity variation in deriving an angular diameter (θ) by first fitting a notional uniform-disc (UD) model. Although this simple formulation fits reasonably well up to the first visibility null, it fails to reproduce the amplitude of the second lobe, which can be seen in the blue dash-dotted line of Fig. 2. This discrepancy confirms the need to account for limb darkening (LD), the physical phenomenon in which the stellar disc intensity drops off towards the limb due to geometrical and atmospheric effects. The fitted uniform-disc angular diameter ($\theta_{\rm UD}$) nonetheless serves as a lower bound on the true angular diameter.

To model the visibility data more accurately, particularly in the higher spatial frequency regime where LD effects are pronounced, we employed the four-term non-linear LD intensity profile, $I(\mu)$, introduced by Claret (2000):

$$\frac{I(\mu)}{I(1)} = 1 - \sum_{k=1}^{4} a_k \left(1 - \mu^{k/2}\right). \tag{1}$$

Here, $\mu = \cos\gamma$, γ is the angle between the line of sight and the stellar surface normal, and a_k are the LD coefficients. This formulation improves upon the simple linear LD profile (Schwarzschild & Villiger 1906),

$$\frac{I(\mu)}{I(1)} = 1 - u(1-\mu), \tag{2}$$

which could not sufficiently reproduce the models of Claret & Bloemen (2011) and the intensity profiles observed by Klinglesmith & Sobieski (1970).

The van Cittert–Zernike theorem (van Cittert 1934; Zernike 1938) relates the intensity distribution of a source to its corresponding fringe visibility via a Fourier transform. Following the approach of Quirrenbach et al. (1996) for a generalized polynomial LD law, the visibility corresponding to equation (1) is calculated as

$$V(x) = 2\frac{\left(1 - \sum_{k=1}^{4} a_k\right)\frac{J_1(x)}{x} + \sum_{k=1}^{4} a_k 2^{k/4}\Gamma\left(\frac{k}{4}+1\right)\frac{J_{k/4+1}(x)}{x^{k/4+1}}}{\left(1 - \sum_{k=1}^{4}\frac{k a_k}{k+4}\right)}. \tag{3}$$

Here, $x = \pi\theta_{\rm LD}\frac{B}{\lambda}$, with B the projected baseline, $\theta_{\rm LD}$ the limb-darkened angular diameter, λ the observing wavelength, $\Gamma(z)$ the gamma function, and $J_n(x)$ the nth-order ordinary Bessel function of the first kind. The quantity $\frac{B}{\lambda}$ is the spatial frequency.

We tested two approaches to determining $\theta_{\rm LD}$. First, we used the STAGGER grid of *ab initio* 3D hydrodynamic stellar atmosphere models (Magic et al. 2013) to obtain theoretical LD coefficients, a_k (Magic et al. 2015), based on the spectroscopic parameters of κ Cyg (see section 2). Consistent with previous studies (e.g., Huber et al. 2012; Karovicova et al. 2020), we adopted coefficients corresponding to the Johnson R band (≈ 670 nm), which is close to the central PAVO wavelength. Using the STAGGER coefficients, we fit our visibility data to equation (3) to determine $\theta_{\rm LD}$. This is shown in Fig. 2 as a red dashed line. Although it fits significantly better than the UD prescription, it underestimates the amplitude of the second lobe, indicating that the models predict stronger limb darkening than is observed.

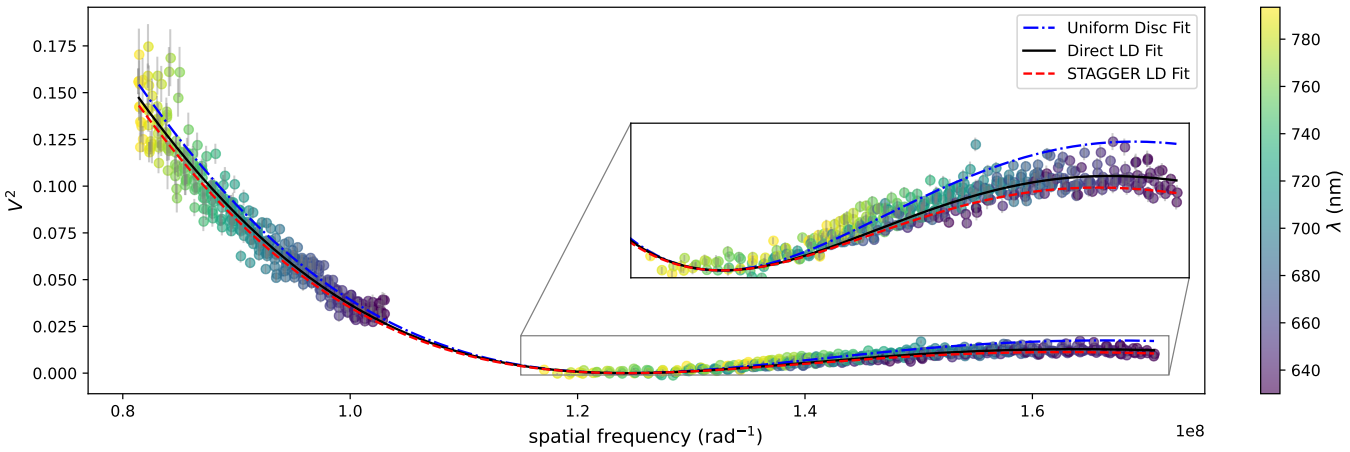

Figure 2. Squared visibility of κ Cyg as a function of spatial frequency, colour-coded by wavelength. The blue dash-dotted line shows the uniform-disc (UD) model, the black solid line shows the direct LD fit, and the red dashed line shows the STAGGER grid limb-darkening (LD) fit. The inset is shown for visual clarity.

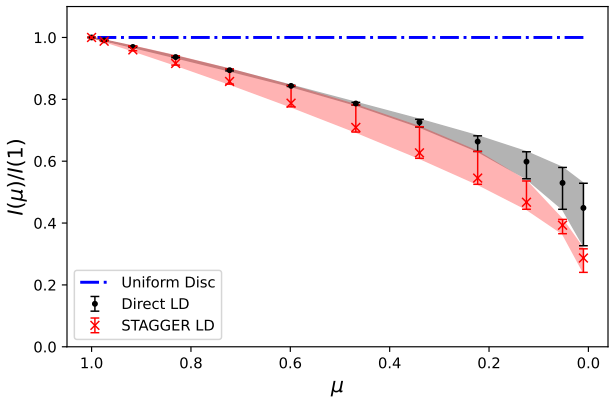

Figure 3. Centre-to-limb intensity variation corresponding to the three cases shown in Fig. 2.

Second, as an alternative to using the 3D models, we performed a direct fit of equation (3) to the observations, treating the a_k and $\theta_{\rm LD}$ as five free parameters. To ensure the physical realism of the derived coefficients, we enforced three constraints that are based on the expected behaviour of stellar intensity:

- the intensity across the entire stellar disc must be positive: $I(0 \leq \mu \leq 1) > 0$.
- the intensity must decrease monotonically from the centre to the limb, i.e. $I(\mu)$ is an increasing function, $\frac{\partial I}{\partial \mu} > 0$.
- the rate of intensity drop should be sharper near the limb than at the centre, i.e. $\frac{\partial^2 I}{\partial \mu^2} \leq 0$.

This constrained fit successfully reproduces the visibility amplitudes in the second lobe (black solid line in Fig. 2). We compare the centre-to-limb intensity variations ($I(\mu)/I(1)$) corresponding to our direct fit and the STAGGER-based fit in Fig. 3, with the UD shown for reference. The direct fit exhibits weaker LD, resulting in a better match to the high spatial-frequency visibility data.

We present the angular diameters and physical radii (R) from the three methods in Table 3. Following Cunha et al. (2007), we calculated the radius using the *Gaia* DR3 parallax (Gaia Collaboration 2022), ϖ, as

$$\frac{R}{\mathrm{R}_\odot} = 107.47 \frac{\theta_{\rm LD}}{\varpi} \tag{4}$$

For completeness, we also mention the results from using a linear LD profile (i.e. equation (2)). The stronger LD predicted by the STAGGER grid produces R approximately 2.1 per cent higher than the direct fit. Because high spatial frequency visibilities are very sensitive to the intensity profile, directly adopting theoretical coefficients without sampling the second lobe can systematically bias the radius measurements (Kervella et al. 2017). Similar discrepancies in the centre-to-limb intensity profiles have been noted in transit studies of dwarfs, and have been attributed to not including the magnetic induction equation in the hydrodynamic models (Maxted 2023; Kostogryz et al. 2024; Verma et al. 2024). We plan to explore this systematic difference of models predicting higher LD in a forthcoming study of other targets that have visibility measurements from PAVO beyond the first null.

3.3 Bolometric Flux

We determined the bolometric flux ($F_{\rm bol}$) and luminosity (L) of κ Cyg by fitting its spectral energy distribution (SED). We compiled a comprehensive set of spectrophotometric measurements from Ducati 2002; Cutri et al. 2003; Ammons et al. 2006; Gaia Collaboration 2022. The adopted magnitudes and corresponding fluxes are listed in Table 4. We assigned an uncertainty of 0.05 mag to the optical bands and employed the reported uncertainties from the sources for the remaining bands. To compare observations with theory, we used Phoenix stellar atmosphere models (Allard et al. 2011, 2012). We integrated these model fluxes over the response curves of each filter to produce synthetic fluxes. The filter transmission functions and zero points were taken from Bessell (2000) for $UBVRI$, Bessell et al. (1998) for $JHKL$ and Evans et al. (2018) for *Gaia* G band. To account for interstellar extinction, we used the wavelength-dependent reddening relations from Cardelli et al. (1989), and the reddened synthetic fluxes were fitted to the observed ones. The best fit (with reddening, $A_v = 0.03$ mag) is shown in dark grey in Fig. 4.

Next, we integrated the fitted SED over wavelength using the trapezoidal rule to obtain $F_{\rm bol}$. Since κ Cyg has very low flux outside the region covered by Phoenix spectra (200–3000 nm), we extrap-

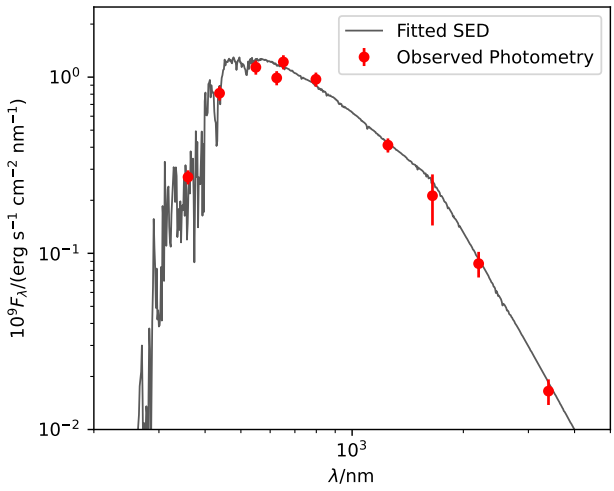

Figure 4. Spectral energy distribution of κ Cyg based on available spectrophotometry, shown as red dots. The best-fit Phoenix spectral template is shown in dark grey.

olated the fitted spectrum following Wien's approximation in the bluer part and Rayleigh-Jeans law in the redder part. The uncertainty on $F_{\rm bol}$ includes systematic effects associated with photometric calibration, extrapolation of fitted SED beyond the observed wavelength range, photometric errors, and interstellar extinction. Therefore, we determined an uncertainty on $F_{\rm bol}$ using Monte Carlo resampling, where the relevant parameters were perturbed within their respective uncertainties, and found a value of 2.3 per cent. Our calculated flux is $F_{\rm bol} = (9.98 \pm 0.24) \times 10^{-7}$ erg s^{-1} cm^{-2}. We adopt this value for our analysis. We cross-checked our calculation with the stellar spectral atlas of Pickles (1998) and obtained $F_{\rm bol} = (9.71 \pm 0.24) \times 10^{-7}$ erg s^{-1} cm^{-2}, which is lower by around 2.7 per cent. A similar offset in the same direction was observed for late K and M dwarfs by Mann et al. (2013).

We calculated luminosity using the inverse square relation, $L = 4\pi d^2 F_{\rm bol}$, where d is the distance of the star, calculated as the inverse of parallax, ϖ. This yields $L = (44.46 \pm 1.09)\ L_\odot$.

Once we have $\theta_{\rm LD}$, we can find the effective temperature of the star by inverting the Stefan-Boltzmann law (van Belle et al. 1999) as

$$T_{\rm eff} = \left(\frac{4F_{\rm bol}}{\sigma \theta_{\rm LD}^2} \right)^{\frac{1}{4}},$$

where σ is the Stefan–Boltzmann constant. The computed vallues of $T_{\rm eff}$, using the different LD prescriptions explained in section 3.2, are listed in Table 3. Because the STAGGER-based fit yields a larger θ_{LD}, the derived $T_{\rm eff}$ is correspondingly lower by about 1 per cent. For the present analysis, we adopt R and $T_{\rm eff}$ obtained using the direct fit pertaining to the four-parameter non-linear LD law, i.e. LD4 (Direct) of Table 3.

4 ASTEROSEISMOLOGY

4.1 Observations

Our asteroseismic analysis relies on high-precision photometry obtained by the *Transiting Exoplanet Survey Satellite* (*TESS*; Ricker et al. 2015). *TESS* observed κ Cyg with a sampling cadence of 120 s across 17 sectors over six years. We used the light curve from the Science Performance Operation Center (SPOC) pipeline, which we

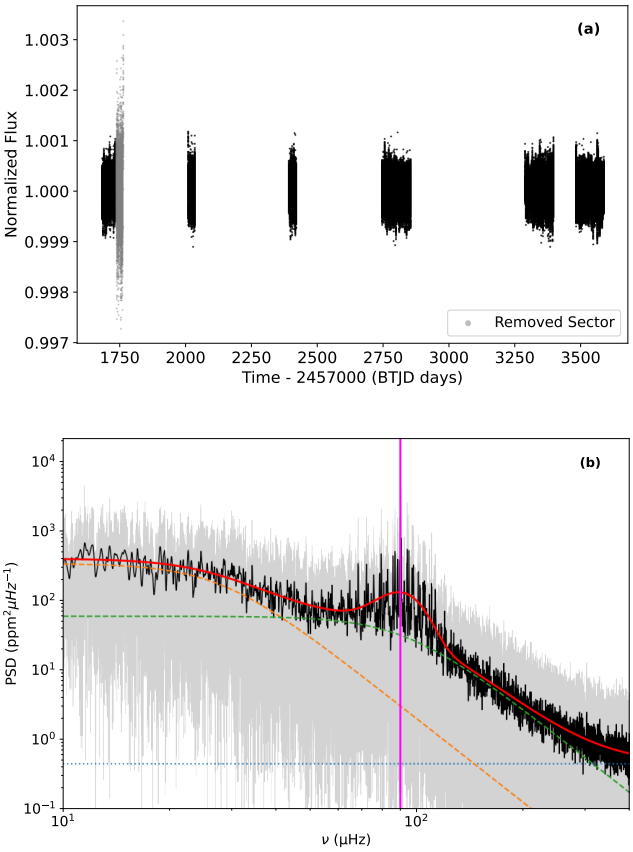

Figure 5. (a) The light curve of κ Cyg with 16 sectors of *TESS* data, processed by the SPOC pipeline. Sector-16 *TESS* data (shown in grey) were omitted because there was a dead pixel column in the TPF. **(b)** The power spectral density (PSD) of κ Cyg with the granulation background noise being modelled using two Harvey functions, shown in orange and green dashed lines. The horizontal dark-blue dotted line represents the white noise. $\nu_{\rm max}$ is shown in a vertical magenta line, and the total PSD fit is shown in a solid red line.

downloaded from MAST using the lightkurve package (Lightkurve Collaboration et al. 2018). Prior to analysis, the data from Sector 16 were removed since they were affected by a dead pixel column. This left us with a clean dataset spanning 16 sectors, shown in Fig. 5a.

We calculated the power spectrum using the Lomb-Scargle method (VanderPlas 2018), oversampled by a factor of 15 relative to the total observation time, and normalised to a power spectral density (PSD) following Parseval's theorem. We modelled the PSD as the sum of white noise from photon statistics (P_w), two super-Lorentzian Harvey-like components describing granulation (following Kallinger et al. 2014), and a Gaussian envelope representing the oscillation power excess. The full model is given by

$$P(\nu) = P_w + \sum_{i=1}^{2} \left[\frac{a_i^2/b_i}{1 + (\nu/b_i)^4} \right] + P_g \exp\left[-\frac{(\nu - \nu_{\rm max})^2}{2\sigma^2} \right], \qquad (5)$$

where a_i are the rms amplitudes, and b_i are their corresponding characteristic frequencies ($\approx (2\pi\tau_i)^{-1}$, with τ_i being the characteristic granulation timescales). The Gaussian term has height P_g, central frequency $\nu_{\rm max}$, and width σ. All the components were fitted to the PSD simultaneously to avoid biases in the determination of $\nu_{\rm max}$. The resulting fit is shown in Fig. 5b. The oscillation power excess is well defined, exhibiting a clear Gaussian envelope with regularly spaced

Method	u	$\theta_{\rm LD}$ (mas)	R ($R_\odot$)	$T_{\rm eff}$ (K)
UD	0	2.027 ± 0.001	8.23 ± 0.01	5196 ± 33
LD4 (STAGGER)	-	$2.176^{+0.007}_{-0.037}$	$8.83^{+0.07}_{-0.11}$	5015^{+60}_{-49}
LD1 (STAGGER)	$0.621^{+0.019}_{-0.046}$	$2.196^{+0.007}_{-0.016}$	$8.90^{+0.07}_{-0.09}$	4992^{+54}_{-48}
LD4 (Direct)	-	$2.132^{+0.007}_{-0.005}$	$8.65^{+0.10}_{-0.10}$	5066^{+47}_{-50}
LD1 (Direct)	$0.393^{+0.005}_{-0.005}$	$2.125^{+0.002}_{-0.002}$	$8.63^{+0.04}_{-0.04}$	5075^{+41}_{-41}

Table 3. Angular diameters ($\theta_{\rm LD}$), physical radii (R) and temperatures ($T_{\rm eff}$) from different methods. UD denotes uniform-disc, LD1 a linear limb-darkening (LD) with coefficient u, and LD4 a four-parameter LD. The LD4 coefficients are not listed, as their numerical values are not directly informative (see Fig. A1). The corresponding intensity profiles for LD4 are shown in Fig. 3.

.

Filter (λ (nm))	U (360)	B (450)	V (555)	R (670)	G (673)	I (870)	J (1220)	H (1630)	K (2190)	L (3500)
mag	5.47(5)	4.73(5)	3.76(5)	3.13(5)	3.54(5)	2.66(5)	2.21(2)	1.82(18)	1.64(1)	1.58(9)
Flux (10^{-9} erg s^{-1} cm^{-2} nm^{-1})	2.71(25)	8.11(75)	11.4(10)	12.2(11)	9.90(91)	9.72(90)	4.11(38)	2.12(68)	0.87(15)	0.17(3)

Table 4. Photometric magnitudes and fluxes of κ Cyg from literature with wavelengths in nm for each filter.

modes, allowing a reliable determination of the global asteroseismic parameters.

4.2 Global Parameters

The overall properties of solar-like oscillators are characterized by two global asteroseismic parameters: the frequency of maximum power ($\nu_{\rm max}$) and the large frequency separation ($\Delta\nu$). The power excess of solar-like oscillations has a characteristic Gaussian envelope, the central frequency of which is denoted by $\nu_{\rm max}$. Brown et al. (1991) argued that $\nu_{\rm max}$ scales as the acoustic cut-off frequency ($\nu_{\rm ac}$) for solar-like oscillators, leading Kjeldsen & Bedding (1995) to posit the following scaling relation:

$$\nu_{\rm max} \propto g T_{\rm eff}^{-0.5}. \tag{6}$$

As mentioned in section 4.1, we determined $\nu_{\rm max}$ by simultaneously fitting a Gaussian function along with the background noise to the PSD. We measured $\nu_{\rm max} = 90.3 \pm 1.9$ μHz. The quoted uncertainties were derived from the scatter observed when determining $\nu_{\rm max}$ for individual *TESS* visits across the analysed sectors (following Sreenivas et al. 2024).

The parameter $\Delta\nu$ is defined as the average frequency spacing between acoustic modes of the same angular degree ℓ and consecutive radial orders n in the asymptotic regime ($n \gg \ell$). It is proportional to the inverse of the sound travel time across the stellar diameter and serves as a robust probe to the mean stellar density (Ulrich 1986). This gives us the other asteroseismic scaling relation:

$$\Delta\nu \propto \sqrt{\frac{M}{R^3}}. \tag{7}$$

We measured $\Delta\nu = 7.42 \pm 0.04$ μHz for κ Cyg using the autocorrelation of its power spectrum. Acoustic glitches can introduce systematic variations in $\Delta\nu$ (Gough 1990; Vrard et al. 2015; Verma et al. 2022) and so, to validate this measurement, we also fitted a straight line to the radial ($\ell = 0$) mode frequencies as a function of radial order. Following the prescription of White et al. (2011), we weighted the fit by a Gaussian envelope centred on $\nu_{\rm max}$, and determined $\Delta\nu = 7.42 \pm 0.03$ μHz, emphasizing the robustness of $\Delta\nu$ determination.

Using the fundamental solar parameters from Huber et al. (2011) ($\nu_{\rm max,\odot} = 3090 \pm 30$ μHz, $\Delta\nu_\odot = 135.1 \pm 0.1$ μHz), plus $T_{\rm eff,\odot} = 5772.0 \pm 0.8$ K (Prša et al. 2016), we estimate the mass (M) and radius (R) of κ Cyg by inverting the scaling relations (Stello et al. 2008; Kallinger et al. 2010) as:

$$\frac{R}{R_\odot} \approx \left(\frac{\nu_{\rm max}}{\nu_{\rm max,\odot}}\right)\left(\frac{\Delta\nu}{\Delta\nu_\odot f_{\Delta\nu}}\right)^{-2}\left(\frac{T_{\rm eff}}{T_{\rm eff,\odot}}\right)^{0.5} \tag{8}$$

and

$$\frac{M}{M_\odot} \approx \left(\frac{\nu_{\rm max}}{\nu_{\rm max,\odot}}\right)^{3}\left(\frac{\Delta\nu}{\Delta\nu_\odot f_{\Delta\nu}}\right)^{-4}\left(\frac{T_{\rm eff}}{T_{\rm eff,\odot}}\right)^{1.5}. \tag{9}$$

The correction factor $f_{\Delta\nu}$ (which accounts for deviations from equation (7)) is typically close to unity. It was estimated for RGB stars by Li et al. (2023) and, using a similar prescription, for CHeB stars by Schimak et al. (2026). Using the latter, with $T_{\rm eff} = 5066^{+47}_{-50}$ K from section 3.3 and [Fe/H] $= 0.10 \pm 0.07$ from section 2, we obtained $f_{\Delta\nu} = 0.995 \pm 0.002$. This gives $R = 8.96 \pm 0.22$ $R_\odot$ and $M = 2.19 \pm 0.16$ $M_\odot$. These values provide the initial constraints for the detailed stellar modelling of κ Cyg discussed in section 5.1.

4.3 Individual Modes

The identification of individual oscillation mode frequencies ($\nu_{n,\ell}$) is essential for detailed stellar modelling beyond scaling relations. To extract the mode frequencies, we used the background-divided power spectrum from section 4.1. We obtained initial estimates of mode frequencies using a peak-finding algorithm implemented in SciPy (Virtanen et al. 2020), applied to a smoothed version of the PSD. The power spectrum of a stochastically excited, damped oscillation has a Lorentzian profile (Anderson et al. 1990), and we fitted this function to the background-divided PSD (García Saravia Ortiz de Montellano et al. 2018) within a $0.01\Delta\nu$ window centred on each detected peak:

$$P(\nu) = \frac{H}{1 + \left(\frac{2(\nu - \nu_0)}{\Gamma}\right)^2}. \tag{10}$$

$P(\nu)$ is the background-divided power spectrum, H is the mode height above the background (dimensionless), ν_0 is the mode fre-

quency, and Γ is the full-width at half-maximum, related to the mode lifetime τ as $\Gamma = (\pi\tau)^{-1}$.

Uncertainties on the individual mode frequencies were estimated from the posterior distributions of a Markov Chain Monte Carlo (MCMC) sampler. We carried out the mode identification based on the asymptotic relation,

$$\nu_{n,l} \simeq \Delta\nu \left(n + \frac{l}{2} + \epsilon_p(n,\ell) \right), \tag{11}$$

where n and ℓ are the radial order and angular degree of the mode, respectively, and $\epsilon_p(n,\ell)$ is the phase offset. A complete list of oscillation mode frequencies detected in κ Cyg is given in Table 5.

For evolved stars like κ Cyg, the oscillation modes have a mixed character, resulting from the coupling between pressure (p) modes in the envelope and gravity (g) modes in the core. In the asymptotic regime, while p-modes are equally spaced in frequency by $\Delta\nu$, the g-modes are equally spaced in period, defined by the g-mode period spacing for degree ℓ as $\Delta\Pi_\ell$. It is known that $\Delta\Pi_1$ is a diagnostic of the internal structure, particularly distinguishing between red giant branch (RGB) stars and core helium-burning (CHeB) clump stars (Bedding et al. 2011; Kallinger et al. 2012; Mosser et al. 2012). To focus our attention majorly of the stellar envelope, we decouple these mixed modes and isolate the pure p-mode characteristics (the π-modes) and the pure g-mode characteristics (the γ-modes) (Ong & Basu 2020; Ong & Gehan 2023), we computed the stretched period (τ) (Mosser et al. 2015) and stretched frequency (f) (Schimak et al. 2026, Li et al. 2024, Y. Li et al, in prep). We calculated the Fourier transform of the stretched period power spectrum, and its maximum amplitude corresponds to $\Delta\Pi_1$. We obtained $\Delta\Pi_1 = 263.3 \pm 2.4$ s. The uncertainty was calculated using the formula for dense mixed-mode pattern from (Vrard et al. 2016). The high value of $\Delta\Pi_1$ identifies κ Cyg as a CHeB star, and its high $\Delta\nu$ of $7.42 \pm 0.04\mu$Hz (see section 4.2) confirms that it is a secondary red clump star (Bedding et al. 2011).

We determined the mode parameters (acoustic phase offset ϵ_p, buoyancy phase offset ϵ_g and mode coupling strength q) by simultaneously aligning the γ-modes vertically in the stretched period échelle diagram and the π-modes vertically in the stretched frequency échelle diagram. The best-fit parameters correspond to minimal deviations of ϵ per acoustic radial order in both échelle diagrams. We adopt the corresponding standard deviations as the uncertainties on respective π and γ modes. The resulting diagrams are shown in Fig. 6. We also note that there is a buoyancy "glitch", which causes curvature in the stretched period diagram, as seen in the third panel of Fig. 6. This is related to the sharp variations in the Brunt–Väisälä frequency profile in clump stars, owing to strong chemical gradients (Cunha et al. 2019; Vrard et al. 2022; Matteuzzi et al. 2025).

For subsequent stellar modelling, we do not use the mixed-mode frequencies, as these strongly depend on the assumptions about core structure and convective boundary mixing, which govern g-mode properties and their coupling to p-modes. By contrast, acoustic waves, being largely confined to the outer envelope, are predominantly sensitive to envelope structure, and less so to the inner radiative regions. We therefore fitted our stellar models using the extracted frequencies of these $\ell = 1$ π-modes.

n_p	$\nu_{n,0}$ (μHz)	$\nu_{n,1,\mathrm{mixed}}$ (μHz)	$\nu_{n,1,\pi}$ (μHz)	$\nu_{n,2}$ (μHz)
7	53.833(127)	56.221(98) 56.967(98) 57.548(60)	56.91(13)	
8	61.188(107)	63.918(80) 64.618(65) 65.411(114)	64.88(18)	67.238(86)
9	68.272(29)	71.073(71) 72.001(59) 72.884(88)	72.00(10)	74.771(238)
10	75.475(52)	77.080(160) 78.392(52) 79.340(40) 80.599(59)	78.85(11)	81.997(176)
11	82.711(42)	85.624(33) 86.776(31) 88.179(31)	86.80(6)	89.403(32)
12	90.254(15)	92.028(58) 93.780(27) 94.915(23)	94.34(26)	96.906(37)
13	97.653(164)	100.901(44) 102.037(69)	101.53(7)	104.255(201)
14	105.241(197)	106.470(142) 108.553(89) 110.043(35)	109.00(22)	
15	112.628(51)			

Table 5. Oscillation mode frequencies for κ Cyg.

5 MODELLING

5.1 Description of the models

To interpret the asteroseismic and interferometric observations of κ Cyg, we computed two extensive grids of stellar evolutionary models using the open-source software, Modules for Experiments in Stellar Astrophysics (MESA, version r24.03.1:Paxton et al. 2011, 2013, 2015, 2018, 2019; Jermyn et al. 2023).

We evolved all evolutionary tracks from the pre-main sequence through to the CHeB phase with resolution settings of `time_delta_coeff` = 0.5, and `mesh_delta_coeff` = 0.5, corresponding to approximately a factor of two increase in both temporal and spatial resolutions relative to the default MESA settings. We terminated the models when the core He mass fraction dropped to 10^{-5}, indicating evolution to the AGB phase. We used the `pp_cno_extras_o18_ne22.net` nuclear network to model the reactions and isotopes relevant to this advanced evolutionary state. To include the outer layers of the atmosphere in the models, we integrated the atmospheric boundary conditions out to an optical depth of $\tau = 10^{-3}$, employing the standard grey atmosphere Eddington $T - \tau$ relation (Eddington 1926), and ensuring opacity consistent with the local temperature and pressure throughout the atmosphere.

The treatment of convective boundaries in CHeB stars remains a key source of systematic uncertainty, affecting predictions of core size, mixing, and evolutionary timescales (e.g., Constantino et al. 2015; Bossini et al. 2017; Paxton et al. 2018; Noll et al. 2024). To explore the impact of these uncertainties, we computed two grids using different convective boundary-mixing prescriptions. The first grid (hereafter grid-PM) adopts MESA's predictive mixing (PM) prescription (Paxton et al. 2018), while the second grid (grid-OS) uses the more commonly employed exponential overshooting (OS) prescription (e.g., Paxton et al. 2011; Moravveji et al. 2016; Pérez Hernández et al. 2019).

Both PM and OS locate the formal convective boundary at the point where $y = \nabla_{\mathrm{rad}} - \nabla_{\mathrm{ad}}$ changes sign (Schwarzschild criterion; Schwarzschild 1958). However, they extend the convective region

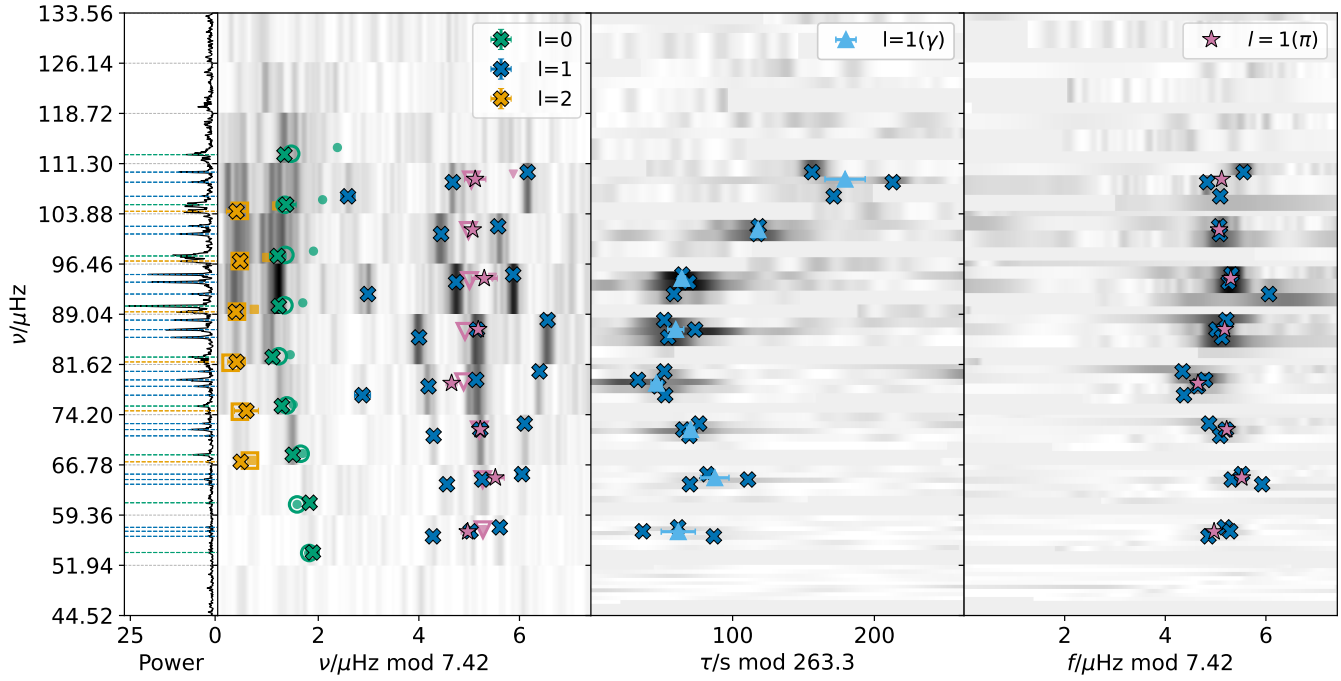

Figure 6. The échelle diagrams of κ Cyg. **Left:** Background-divided power spectrum with identified modes, shown in vertical dashed lines, green for radial, dark blue for mixed dipolar and orange for quadrupolar modes. **Second:** Corresponding frequency échelle diagram showing the observed modes with crosses and pure $l = 1$ π-modes in pink stars. Filled symbols are used for modelled frequencies, and the surface-corrected ones are shown with empty symbols (circle for $\ell = 0$, inverted triangle for $\ell = 1$ and square for $\ell = 2$). **Third:** Corresponding stretched period échelle diagram for the dipolar modes showing the pure $l = 1$ γ-modes in light blue. **Right:** Corresponding stretched frequency échelle diagram for the dipolar modes. We have masked out the radial and quadrupolar modes for better visualization in the stretched échelle diagrams.

beyond the formal limit in distinct ways to account for the momentum of convective motions near this boundary.

PM checks how superadiabatic the first cell (the "candidate cell") on the notional radiative side is and mixes it so that it has the same composition as the adjacent cell on the convective side. Then it recomputes y, and if $y > 0$ on both sides of the convective boundary, the next cell becomes the "candidate cell". This is repeated until the candidate cell has $y < 0$ after the proposed mixing (Paxton et al. 2018).

The convective OS is assumed to be diffusive (Zhang 2013), and for the exponential prescription (Herwig 2000), it extends the mixed region by an exponentially decreasing diffusion coefficient beyond the formal convective boundary, depending on the overshoot parameter, $f_{\rm ov}$ (Paxton et al. 2011).

For both grids, the initial set of parameters was distributed quasi-randomly across the parameter space using a Sobol sequence (Sobol 1967) to ensure efficient non-Cartesian exploration of the parameter space (grid-PM: $2^{12} = 4096$ models; grid-OS: $2^{10} = 1024$ models). The following parameters are standardized across both grids:

- **Initial Mass ($M_{\rm ini}$):** We constrained the search to a mass range centred on the scaling relation mass from section 4.2. We restricted the grid to $M_{\rm ini} \in [2.0, 2.8]$ $M_\odot$.
- **Metallicity ($Z_{\rm ini}$):** We varied the initial metallicity in the range $Z_{\rm ini} \in [0.015, 0.03]$, which corresponds to [Fe/H] $\in [-0.13, 0.17]$, adopting the solar composition from Grevesse & Sauval (1998). This covers the range expected from spectroscopic measurements, mentioned in section 2.
- **Helium Abundance ($Y_{\rm ini}$):** Since the helium abundance is difficult to constrain spectroscopically due to the absence of He absorption lines in the spectra, we varied $Y_{\rm ini}$ from 0.25 to 0.35. It covers a broader range than what the primordial He enrichment law mentioned in Li et al. (2018) provides. This was done since this enrichment law is often said to be an oversimplification (Nsamba et al. 2021).
- **Mixing Length ($\alpha_{\rm MLT}$):** Convection was treated using the standard Mixing Length Theory (MLT; Böhm-Vitense 1958; Cox & Giuli 1968) in which convective transport is approximated as a diffusive process with characteristic length-scale $\alpha_{\rm MLT} H_P$. Here, H_P is the local pressure-scale height and $\alpha_{\rm MLT}$ is a free parameter that directly controls the efficacy of convective energy transport and strongly influences R and $T_{\rm eff}$. $\alpha_{\rm MLT}$ is typically calibrated against the Sun, yielding $\alpha_{\rm MLT} \approx 1.92$ for a standard solar model (Paxton et al. 2011; Joyce & Chaboyer 2018), but observations of evolved stars indicate that non-solar values of $\alpha_{\rm MLT}$ are often required to reproduce their global properties (Piau et al. 2011; Ball & Gizon 2017; Tayar et al. 2017; Li et al. 2018). Hence, we allowed $\alpha_{\rm MLT}$ to vary over a wide range (1.6 – 2.3) in our model grid.
- **Mass Loss (η):** Mass loss near the tip of RGB affects the mass of the CHeB star, although less so for the more massive stars since their RGB lifetime is short and hence the integrated mass loss is low (Girardi 1999). However, we included RGB mass loss using the Reimers (1975) prescription to check whether our results are sensitive to plausible uncertainties in mass-loss efficiency. Following the cluster analysis by Miglio et al. (2012), we varied the efficiency parameter over $\eta \in [0.1, 0.3]$.

Next, we considered grid-specific parameters that can potentially influence our results:

- **`predictive_superad_thresh`** (for grid-PM only): The formal boundary of PM is defined using

`predictive_superad_thresh` where the mixing stops if $\frac{\nabla_{\rm rad}}{\nabla_{\rm ad}} - 1$ drops below this threshold instead of 0 (from Schwarzschild criterion; Schwarzschild 1958). To minimize the occurrence of core breathing pulses and splitting of the convective core (Paxton et al. 2018, 2019; Ostrowski et al. 2021), we varied `predictive_superad_thresh` from 0 to 0.025, covering the suggested value for CHeB stars (Paxton et al. 2018).

- **Overshooting ($f_{\rm ov}$)** (for grid-OS only): We employed the commonly adopted exponential overshooting scheme, varying $f_{\rm ov} \in [0.0001 - 0.025]$ at the boundaries between radiative and convective zones in the core and envelope.

We computed the corresponding theoretical adiabatic oscillation frequencies using the pulsation code GYRE (Townsend & Teitler 2013; version 7.1), as implemented within MESA's `run_star_extras modules` (Bellinger 2022). We searched for frequencies on a linear grid between 30 and 140 μHz, covering the full observed oscillation envelope around $\nu_{\rm max}$. The scan used 200 trial frequencies for radial modes and 1000 trial frequencies for $\ell = 1, 2$ modes. We used the pure π-mode prescription from Ong & Basu (2020) for $\ell = 1, 2$ modes.

5.2 Modelling of κ Cyg

Standard 1D stellar structure models are known to inadequately capture the physical conditions in the near-surface layers of stars, characterized by low density and vigorous, non-adiabatic turbulent motions that are oversimplified in mixing-length theory (Grigahcène et al. 2005). In addition, surface magnetism and non-adiabatic frequency shifts from radiative and convective damping also act predominantly in these layers. These deficiencies introduce a systematic offset in modelled oscillation frequencies, the so-called "surface effect", which can significantly bias the inference of fundamental stellar parameters if left uncorrected.

To mitigate this systematic deviation, we employed the two-term parametric surface correction proposed by Ball & Gizon (2014). Unlike the former empirical power-laws (Kjeldsen et al. 2008), this correction is derived from the theoretical work of Gough (1990) and scales inversely with the normalised mode inertia $I_{n,l}$, which we obtained from GYRE.

We calculated the surface correction term, $\delta\nu_{\rm surf}$, for each model frequency, $\nu_{\rm mod}$, as

$$\frac{\delta\nu_{\rm surf}}{\nu_{\rm ac}} = \frac{1}{I_{n,l}} \left[a_{-1} \left(\frac{\nu_{\rm mod}}{\nu_{\rm ac}} \right)^{-1} + a_3 \left(\frac{\nu_{\rm mod}}{\nu_{\rm ac}} \right)^{3} \right], \tag{12}$$

where $\nu_{\rm ac}$ is the acoustic cutoff frequency, and a_{-1} and a_3 are dimensionless coefficients determined by fitting the corresponding observed mode frequencies, $\nu_{\rm obs}$. For every model in our grid, we determined a_{-1} and a_3 via a linear least-squares fit to the differences between $\nu_{\rm mod}$ and $\nu_{\rm obs}$. We then assessed the goodness-of-fit for each model using a reduced $\chi^2_{\rm red}$ metric defined as

$$\chi^2_{\rm red} = \frac{1}{N-2} \sum_{i=1}^{N} \frac{(\nu_{{\rm obs},i} - \nu_{{\rm mod},i} - \delta\nu_{{\rm surf},i})^2}{\sigma_i^2}, \tag{13}$$

where N is the number of fitted modes, and σ_i are the observational uncertainties on the individual mode frequencies (see Table 5). We further constrained the sign of surface correction so that our analysis retained only the models in which the radial mode frequencies follow the expected trend, similar to solar models (i.e., $\delta\nu_{\rm surf} \leq 0$, and its magnitude increases with frequency). We imposed a constraint on $T_{\rm eff}$ from section 3.3 and on no other parameter to test the asteroseismic performance of our two convective boundary mixing prescriptions. The likelihood for each model was calculated as $\mathcal{L} = \exp\left(-(\chi^2_{\rm red} + \chi^2_{T_{\rm eff}})/2\right)$.

The weighted histograms of the stellar parameters for κ Cyg derived from this process are presented in panels (a), (d) and (g) of Fig. 7. The observed interferometric radius, shown using a grey-shaded patch, shows a significant discrepancy: the modelled radius distributions for both prescriptions of convective boundary mixing are overestimated. The best-fitting models from grid-OS, while marginally closer to the interferometric value, are still systematically higher by about 3.2 per cent. The grid-PM shows a distinct lack of acceptable models capable of reproducing the required radius. The median $T_{\rm eff}$ values from both grids agree with the $T_{\rm eff}$ from section 3.3 within 1 σ. Hence, the luminosity predicted by the models is also higher than what we calculated in section 3.3. The modelled values for κ Cyg using both models are reported in Table 6 and the corner plot correspoding to grid-OS is shown in Fig. B1. To further constrain our system, we considered additional parameters in the likelihood function. Including $\nu_{\rm max}$ did not alter the results, as shown in Table 6 and Fig. B1, where it is accurately reproduced even without constraints. We also explored the use of $\Delta\Pi$ and R as additional constraints; however, the grids did not contain sufficient models to incorporate them meaningfully. The modelled $\Delta\Pi_1$ is smaller than the observed one, in line with previoous studies (e.g., Constantino et al. 2015; Noll et al. 2025). We tested including a third term, linearly dependent on frequency in equation (12). However, this had little impact on our results, indicating that the primary source of the radius discrepancy is unlikely to be the difference in density perturbations confined to the near-surface layers of the models and the actual star.

5.3 Comparison with two *Kepler* analogues

Our difficulties in finding a model of κ Cyg that is consistent with its interferometric radius may indicate either that κ Cyg is anomalous in some fashion, or that secondary clump stars in general are systematically poorly described by stellar models of the kind that we have used. To investigate, we extended our analysis to two bright secondary clump stars observed by the *Kepler* mission (Borucki et al. 2010): HD 226808 ($V = 7.19$) and HD 181827 ($V = 8.67$), the second of which also has an interferometric radius. For both stars, we applied a methodology identical to κ Cyg for mode extraction and grid modelling. The independent measurements used for comparison with the asteroseismic models can be found in Table 6.

5.3.1 The case of HD 226808

HD 226808 (KIC 5307747) is one of the brightest *Kepler* secondary clump stars studied by Mosser et al. (2014). The star has been previously modelled by De Moura et al. (2020), but the modes were misidentified ($\ell = 0$ and $\ell = 1$ ridges were swapped). We prepared its background-divided power spectrum and identified modes using stretched échelle diagrams for π and γ modes, shown in Fig. 8a. We do not see any curvature in the stretched period échelle diagram. We expect this if the star is very early in its CHeB phase and has no sharp density gradient. The full list of its mode frequencies is presented in Table 7. Since high-fidelity interferometry is unavailable for HD 226808, we compared our derived luminosity with that reported in the *Gaia* DR3 catalogue using the FLAME module (Creevey & Lebreton 2022). Contrary to what we observed for κ Cyg, both model grids predict the *Gaia* luminosity quite accurately. Also, we used the

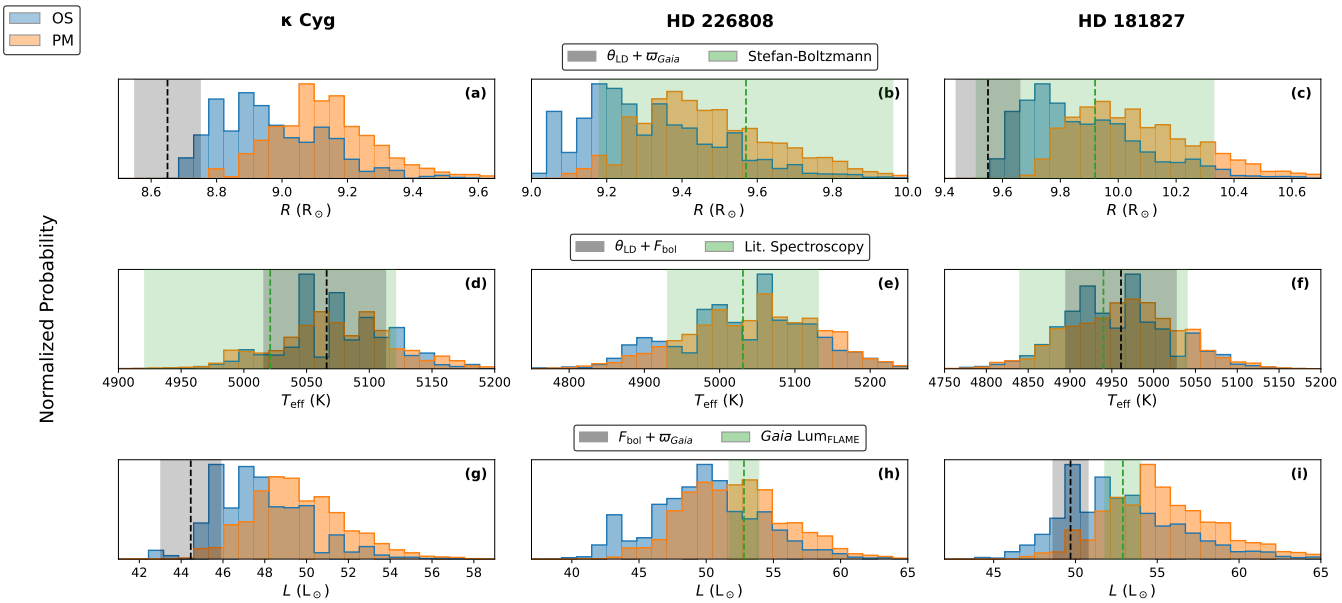

Figure 7. Overall modelling results: blue is for overshooting (OS), and orange is for predictive mixing (PM). **(a-c):** radius distributions. The grey patch is for PAVO radius with *Gaia* parallax, and the green patch is for Stefan-Boltzmann radius using *Gaia* Lum$_{FLAME}$ and spectroscopic T_{eff}. **(d-f):** T_{eff} distributions. The grey patch shows T_{eff} using bolometry and PAVO angular diameter. The green patch is for spectroscopic T_{eff}. **(g-i):** luminosity distributions. The grey patch is L from bolometry and *Gaia* parallax, and the green patch is from *Gaia* Lum$_{FLAME}$.

Source	M ($M_\odot$)	R ($R_\odot$)	T_{eff} (K)	L ($L_\odot$)	Age (Gyr)	ν_{max} (μHz)	$\Delta\Pi_1$ (s)	log g	[Fe/H]
HD 181276 (κ Cyg)									
TESS + PAVO	—	$8.65^{+0.10}_{-0.10}$	5066^{+50}_{-47}	$44.46^{+1.43}_{-1.43}$	—	$90.3^{+1.9}_{-1.9}$	$263.3^{+2.4}_{-2.4}$	$3.02^{+0.08}_{-0.08}$ [a]	$0.10^{+0.07}_{-0.07}$ [a]
Grid (PM)	$2.32^{+0.11}_{-0.08}$	$9.12^{+0.15}_{-0.13}$	5073^{+42}_{-49}	$49.41^{+2.32}_{-2.23}$	$0.68^{+0.12}_{-0.10}$	$92.20^{+1.40}_{-1.08}$	206^{+45}_{-34}	$2.884^{+0.006}_{-0.003}$	$0.04^{+0.09}_{-0.11}$
Grid (OS)	$2.19^{+0.14}_{-0.07}$	$8.93^{+0.21}_{-0.13}$	5077^{+40}_{-41}	$47.55^{+2.27}_{-1.89}$	$0.88^{+0.11}_{-0.15}$	$90.79^{+1.56}_{-0.79}$	208^{+25}_{-39}	$2.878^{+0.007}_{-0.004}$	$0.06^{+0.10}_{-0.13}$
HD 226808 (KIC 5307747)									
Kepler + *Gaia*	—	$9.57^{+0.39}_{-0.39}$	5031^{+100}_{-100}	$52.81^{+1.10}_{-1.10}$	—	$83.4^{+2.3}_{-2.3}$	$290.0^{+1.5}_{-1.5}$	$2.77^{+0.08}_{-0.08}$ [b]	$0.01^{+0.07}_{-0.07}$ [b]
Grid (PM)	$2.26^{+0.14}_{-0.09}$	$9.45^{+0.22}_{-0.15}$	5052^{+82}_{-90}	$52.09^{+3.98}_{-3.67}$	$0.70^{+0.12}_{-0.13}$	$84.02^{+1.72}_{-1.48}$	202^{+68}_{-41}	$2.843^{+0.007}_{-0.005}$	$0.04^{+0.09}_{-0.11}$
Grid (OS)	$2.16^{+0.14}_{-0.09}$	$9.28^{+0.24}_{-0.14}$	5048^{+74}_{-113}	$49.78^{+4.48}_{-3.74}$	$0.89^{+0.21}_{-0.18}$	$82.82^{+1.85}_{-1.41}$	202^{+44}_{-36}	$2.836^{+0.008}_{-0.006}$	$0.06^{+0.08}_{-0.09}$
HD 181827 (KIC 8813946)									
Kepler + PAVO	—	$9.55^{+0.11}_{-0.11}$	4961^{+66}_{-66}	$49.70^{+1.07}_{-1.07}$	—	$73.1^{+2.3}_{-2.3}$	$295.0^{+2.0}_{-2.0}$	$2.81^{+0.08}_{-0.08}$ [c]	$0.14^{+0.07}_{-0.07}$ [c]
Grid (PM)	$2.26^{+0.18}_{-0.10}$	$10.03^{+0.27}_{-0.18}$	4968^{+65}_{-72}	$54.84^{+3.77}_{-2.90}$	$0.69^{+0.12}_{-0.15}$	$75.18^{+1.84}_{-1.24}$	219^{+52}_{-35}	$2.790^{+0.010}_{-0.005}$	$0.06^{+0.08}_{-0.09}$
Grid (OS)	$2.14^{+0.16}_{-0.08}$	$9.82^{+0.27}_{-0.14}$	4948^{+67}_{-50}	$52.41^{+4.13}_{-2.99}$	$0.88^{+0.25}_{-0.18}$	$74.02^{+1.60}_{-1.04}$	225^{+31}_{-36}	$2.784^{+0.009}_{-0.006}$	$0.06^{+0.08}_{-0.09}$

[a] from Deka-Szymankiewicz et al. (2018)
[b] from Takeda & Tajitsu (2015)
[c] from Thygesen et al. (2012)

Table 6. Comparison of observations with asteroseismic modelling results for key stellar parameters of the three targets, obtained using the predictive mixing (PM) and overshooting (OS) prescriptions.

spectroscopic T_{eff} reported from Takeda & Tajitsu (2015) and calculated its radius using the Stefan-Boltzmann law. The distributions of the modelled parameters can be seen in the panels (b), (e) and (h) of Fig. 7. Since an interferometric radius is not available, a direct comparison and a firm conclusion cannot be made.

5.3.2 *The case of HD 181827*

HD 181827 (KIC 8813946) is another secondary-clump star in the *Kepler* field (Mosser et al. 2014). Its global asteroseismic properties and limb-darkened angular diameter, θ_{LD}, were previously measured by Huber et al. (2012). As noted by Huber et al. (2012), there were no data beyond the first null from PAVO interferometry for this star. Hence, we cannot employ our prescription to use the more realistic non-linear LD parametrization. Instead, we use the linear prescription. Motivated by our results for κ Cyg, which suggest that atmospheric models may favour higher limb-darkening coefficients, we imposed a weak Gaussian prior on the linear limb-darkening coefficient (u) centred at 0.4 while fitting the PAVO data for θ_{LD} and u. Our θ_{LD} agreed with the reported interferometric value within 0.5 per cent.

The *Kepler* background-divided power spectrum and échelle di-

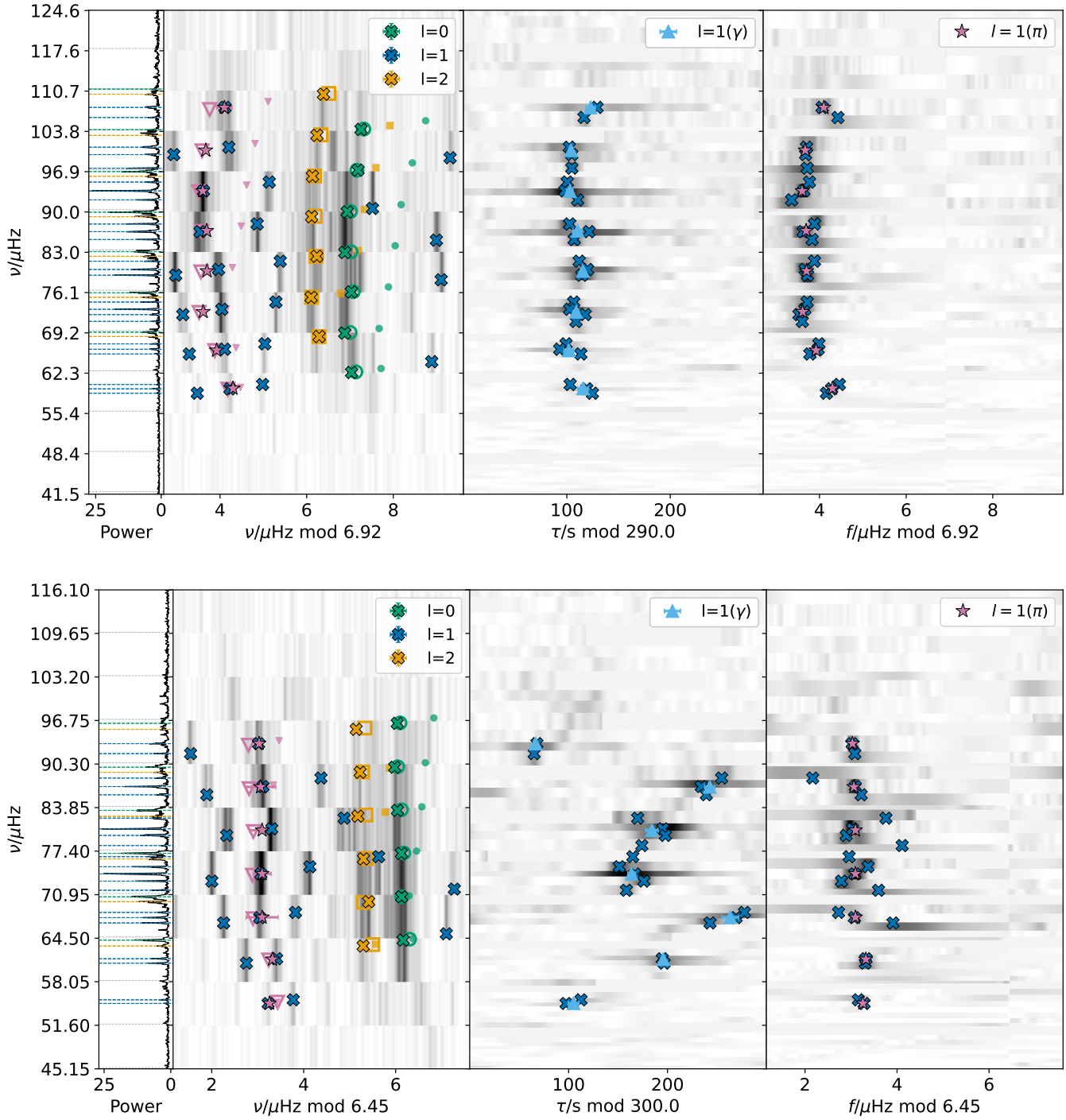

Figure 8. Same as Fig. 6 but for the *Kepler* stars (HD 226808 on top and HD 181827 at bottom). Note that the échelle diagrams have been horizontally shifted for better visualization of the respective ridges.

agrams for this star are shown in Fig. 8b, and the complete set of its observed frequencies is listed in Table 8. As in κ Cyg, we can notice a buoyancy "glitch" in the stretched period échelle diagram of HD 181827.

Using the updated interferometric radius derived from the *Gaia* parallax and the bolometric flux and temperature from Phoenix models (Allard et al. 2011, 2012), we compared our asteroseismic modelling results (panels (c), (f) and (i) of Fig. 7) against these direct constraints. The modelling results for HD 181827 echo the discrepancy encountered with κ Cyg: the model-derived radii are systematically greater than the measured interferometric radius by 3.2 per cent. Hence, the luminosities derived from the model grids are higher than our bolometric calculation. However, the *Gaia* FLAME luminosity agrees quite well with our model grids. Also, the spectroscopic $T_{\rm eff}$ value from Thygesen et al. (2012) matches with what we calculated from bolometry. So, the Stefan-Boltzmann radius for the star, calcu-

n_p	$\nu_{n,0}$ (μHz)	$\nu_{n,1,\mathrm{mixed}}$ (μHz)	$\nu_{n,1,\pi}$ (μHz)	$\nu_{n,2}$ (μHz)
8		58.834(69) 59.587(49) 60.343(56)	59.66(8)	
9		65.570(80) 66.386(40) 67.314(34)	66.20(8)	68.569(45)
10	69.315(82)	71.167(83) 72.342(64) 73.242(19) 74.489(34)	72.81(8)	75.303(88)
11	76.078(45)	79.096(30) 80.085(25) 81.509(30)	79.82(3)	82.356(161)
12	83.153(47)	85.225(27) 86.577(37) 87.898(32)	86.73(7)	89.155(90)
13	89.922(10)	92.035(23) 93.578(19) 95.096(38)	93.56(11)	96.094(130)
14	96.897(27)	97.479(26) 99.813(54) 101.082(55)	100.55(15)	103.118(85)
15	104.065(64)	106.191(33) 107.913(67)	107.90(21)	110.189(54)
16	111.056(110)			

Table 7. Oscillation mode frequencies for HD 226808.

n_p	$\nu_{n,0}$ (μHz)	$\nu_{n,1,\mathrm{mixed}}$ (μHz)	$\nu_{n,1,\pi}$ (μHz)	$\nu_{n,2}$ (μHz)
7		54.828(57) 55.373(37)	54.86(6)	
8		60.806(28) 61.462(25)	61.37(3)	63.343(56)
9	64.213(64)	66.761(26) 67.544(17) 68.322(58)	67.60(25)	69.913(41)
10	70.630(64)	71.602(46) 72.953(19) 74.017(11) 75.085(19) 76.580(52)	74.05(18)	76.250(72)
11	77.075(16)	78.225(71) 79.727(25) 80.706(17) 82.279(64)	80.50(21)	82.578(130)
12	83.439(56)	85.744(42) 86.965(26) 88.226(80)	86.91(15)	89.077(50)
13	89.828(51)	91.841(39) 93.321(52)	93.33(5)	95.441(67)
14	96.334(92)			

Table 8. Oscillation mode frequencies for HD 181827.

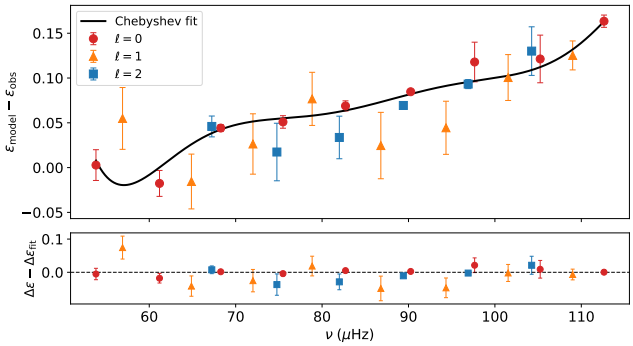

Figure 9. ϵ_p differences between the modelled (best from grid-OS) and observed frequencies along with the residuals from the best ℓ independent Chebyshev polynomial fit.

lated using the *Gaia* FLAME luminosity, is significantly larger than PAVO θ_{LD} and hence much closer to the asteroseismically modelled radius.

Although no independent constraints from interferometry, bolometry, or spectroscopy were imposed on our models, Fig. 7 reveals a clear lack of acceptable models from either grid that reproduce the interferometric radii of κ Cyg and HD 181827.

5.4 Analysis of ϵ_p differences

Following Roxburgh (2016) and Ong et al. (2021), we looked at the differences in ϵ_p (from equation (11)) between the best model and the observed frequencies to infer about the respective internal structures. If the two models share the same interior structure, the ϵ_p differences reduce to a function of ν alone. In contrast, if their internal structures differ, these differences depend on both ℓ and ν.

We first fitted an ℓ-independent Chebyshev polynomial in frequency to the ϵ_p differences, representing the null hypothesis (H0) of no ℓ-dependence (see Fig. 9). To test for potential ℓ-dependent structure (H1), we performed a nested-model comparison, which yields $\Delta\chi^2 = 8.85$ ($p = 0.012$), an F-test $p = 0.079$, ΔAIC = 4.85, and ΔBIC = 2.58, corresponding to weak-to-moderate evidence for ℓ-dependence on the Jeffreys scale (Kass & Wasserman 1995). The $\ell = 1, 2$ modes show a systematic offset from the ℓ-independent fit that is twice in magnitude to the overall weighted scatter. So, we note that the residuals reveal a subtle ℓ-dependent pattern, likely driven by differences between the internal structure of the models and the star, particularly near the core boundary. Similar analyses using the corresponding best models for the two *Kepler* stars show comparable ℓ-dependent signatures.

To diagnose potential differences in the interior structures of these stars, we applied the ϵ_p-difference technique on a star-versus-star basis, between κ Cyg and the two *Kepler* stars. To our knowledge, this is the first time, the ϵ_p-difference technique has been applied in this fashion, differentially between two real stars. We treat κ Cyg as our reference star and each of the *Kepler* stars as targets. The diagrams can be seen in Fig. 10.

In contrast to the star-versus-model comparison, both the reference and target frequency sets carry observational uncertainties. This naturally leads to smaller χ^2 values and therefore somewhat reduced sensitivity to subtle ℓ-dependent signatures. Nevertheless, we apply the same statistical framework to test for ℓ-dependence. For HD 226808, the nested-model comparison yields $\Delta\chi^2 = 0.27$ ($p = 0.876$), F-test $p = 0.856$, ΔAIC = -3.73 and ΔBIC = -5.73, all consistent with an

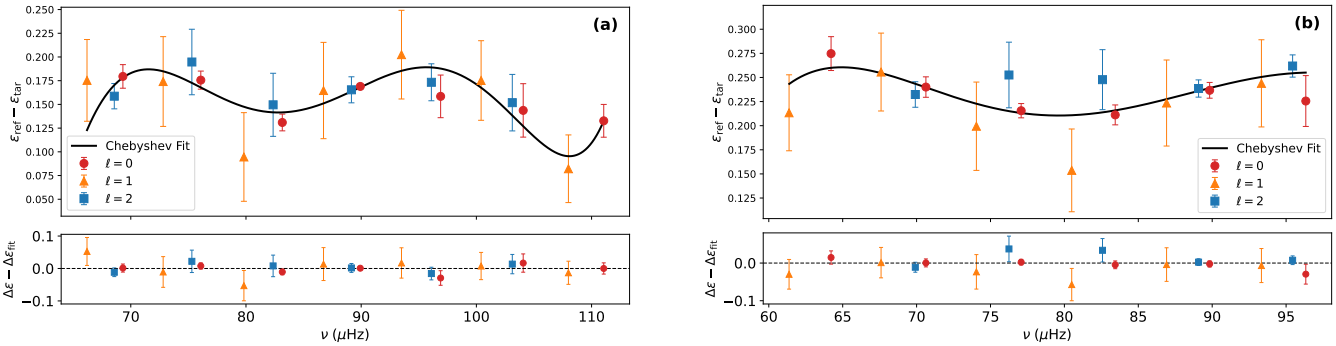

Figure 10. ϵ_p-difference diagrams between: **(a)** κ Cyg and HD 226808 and **(b)** κ Cyg and HD 181827.

ℓ-independent ϵ_p difference. Similarly, for HD 181827, we obtain $\Delta\chi^2$ = 2.01 (p = 0.366), F-test p = 0.301, ΔAIC = -1.99 and ΔBIC = -3.66, consistent with ℓ-independent ϵ_p difference. Hence, we note that within the observational uncertainties, we do not detect a clear ℓ-dependence in the inter-star ϵ_p differences for either target, indicating that their interior structures are broadly comparable to that of κ Cyg. Since it was deduced in section 5.2 that the models do not produce the same core structure as κ Cyg, it is not a surprise that the modelled radius of HD 181827 is higher than the interferometric one.

6 CONCLUSIONS

We have performed the first detailed characterization of the secondary clump star, κ Cyg, by combining high-precision *TESS* asteroseismology with visible-wavelength interferometry using the PAVO beam combiner at the CHARA Array. This dual approach allowed for a stringent test of stellar evolutionary models in the core helium-burning phase, which remains a regime of significant theoretical uncertainty. Our main findings are:

- Squared-visibility measurements beyond the first null allow a direct fit to the four-parameter non-linear limb-darkening law. We found that the 3D hydrodynamic STAGGER model provides a limb-darkened radius for κ Cyg by approximately 2.1 per cent higher than that derived from a direct fit. Using synthetic spectra from Phoenix atmospheric models and spectrophotometric magnitudes of κ Cyg, we calculated $F_{\rm bol}$ by fitting the spectral energy distribution function. We noticed that using Pickles atlas of stellar spectra gives $F_{\rm bol}$ lower by about 2.7 per cent.
- Using 16 sectors of TESS photometry, we identified clear solar-like oscillations in the power spectrum of κ Cyg. By employing stretched-period and stretched-frequency échelle diagrams, we decoupled the mixed dipole modes to extract π-modes, which are sensitive to the acoustic cavity and provide a robust seismic probe that is independent of the complex core-coupling physics.
- We compared the observed oscillation frequencies of κ Cyg against two extensive MESA grids using either predictive mixing or exponential overshooting. Both grids systematically overestimated the stellar radius compared to our interferometric measurement. Although the overshooting grid performed marginally better, it yielded a median radius approximately 3.2 per cent higher than the observed value.
- By repeating our asteroseismic analysis for two *Kepler* secondary clump stars, HD 226808 and HD 181827, we investigated the radius discrepancy observed in κ Cyg. Although the models do reproduce the *Gaia* parameters of HD 226808 accurately, the interferometric radius of HD 181827 is consistently overestimated, as in the case of κ Cyg.
- There is a clear internal inconsistency in current 1D models of secondary clump stars: models that reproduce the envelope-dominated p-mode frequencies systematically predict stellar radii larger than the interferometric measurement. The largely geometric nature of the interferometric radius implies that the models, rather than the observations, are incorrect. This conclusion is further strengthened by the fact that the same models also underpredict the dipole-mode period spacing $\Delta\Pi_1$.

The failure to reproduce both the global radius and the buoyancy-related asteroseismic diagnostics indicates that the internal structure of the models—most likely the treatment of core boundary mixing during and prior to core-helium burning—is not fully realistic. Although we isolated the pure p (π) modes to minimise sensitivity to the core structure and core mixing, the results indicate that some residual influence from the core remains. While the models employed here are representative of the current state of the art in 1D stellar evolution, aided by interferometry, κ Cyg acts as a benchmark to demonstrate that matching envelope-sensitive asteroseismic constraints alone is insufficient to guarantee a correct global or core structure. Future work will focus on expanding the list of secondary clump stars with interferometric data to reconcile the tension between asteroseismic predictions and direct interferometric radii.

ACKNOWLEDGEMENTS

AC, TRB, LSS and CLC acknowledge support from the Australian Research Council through Laureate Fellowship FL220100117. DH acknowledges support from the National Aeronautics and Space Administration (80NSSC22K0781) and the Australian Research Council (FT200100871).

This work uses observations obtained with the Georgia State University Center for High Angular Resolution Astronomy Array at Mount Wilson Observatory. The array is supported by the National Science Foundation under Grant No. AST-1211929 and AST-1411654. Institutional support has been provided from the GSU College of Arts and Sciences and the GSU Office of the Vice President for Research and Economic Development. We have used data collected by the *TESS* and *Kepler* missions and obtained from the MAST data archive at the Space Telescope Science Institute (STScI). Funding for

the *Kepler* mission is provided by the NASA Science Mission Directorate, and for the *TESS* mission by the NASA Explorer Programme. STScI is operated by the Association of Universities for Research in Astronomy, Inc., under NASA contract NAS 5-26555. We use data from the *Gaia* mission, funded by the European Space Agency. This paper has made use of the SIMBAD[1] database (Wenger et al. 2000), operated at CDS, Strasbourg, France.

Software: We have extensively used several public Python packages: NumPy (Harris et al. 2020); Matplotlib (Hunter 2007); SciPy (Virtanen et al. 2020); Astropy (Astropy Collaboration et al. 2013, 2018, 2022); Pandas (Wes McKinney 2010; pandas development team 2020); Emcee (Foreman-Mackey et al. 2013); lightkurve (Lightkurve Collaboration et al. 2018).

This research has used the open-source stellar evolutionary code, Modules for Experiments in Stellar Astrophysics (Mesa, version r24.03.1:Paxton et al. 2011, 2013, 2015, 2018, 2019; Jermyn et al. 2023). The equation of state (EOS) implemented Mesa is constructed from a composite of several sources, including OPAL (Rogers & Nayfonov 2002), SCVH (Saumon et al. 1995), FreeEOS (Irwin 2012), HELM (Timmes & Swesty 2000), PC (Potekhin & Chabrier 2010), and Skye (Jermyn et al. 2021). Radiative opacities are taken primarily from the OPAL tables (Iglesias & Rogers 1993; Itoh et al. 1996), supplemented at low temperatures by Ferguson et al. (2005) and extended to the high-temperature, Compton–scattering–dominated regime using the prescription of Poutanen (2017). Electron conduction opacities follow Cassisi et al. (2007) and Blouin et al. (2020). Nuclear reaction rates are adopted from the JINA REACLIB database (Cyburt et al. 2010), NACRE (Angulo et al. 1999), along with tabulated weak interaction rates from Fuller et al. (1985); Oda et al. (1994); Langanke & Martínez-Pinedo (2000). Coulomb screening is treated using the formulation of Chugunov et al. (2007), while thermal neutrino energy-loss rates are taken from Itoh et al. (1996).

DATA AVAILABILITY

The *TESS* and *Kepler* data underlying this article are available at the MAST Portal (Barbara A. Mikulski Archive for Space Telescopes), at https://mast.stsci.edu/portal/Mashup/Clients/Mast/Portal.html. The stellar visibilities and stellar models (MESA and GYRE inlists) are available under this DOI: https://doi.org/10.5281/zenodo.18971442.

REFERENCES

Aerts C., 2021, Reviews of Modern Physics, 93, 015001
Allard F., Homeier D., Freytag B., 2011, in Johns-Krull C., Browning M. K., West A. A., eds, Astronomical Society of the Pacific Conference Series Vol. 448, 16th Cambridge Workshop on Cool Stars, Stellar Systems, and the Sun. p. 91 (arXiv:1011.5405), doi:10.48550/arXiv.1011.5405
Allard F., Homeier D., Freytag B., Sharp C. M., 2012, in Reylé C., Charbonnel C., Schultheis M., eds, EAS Publications Series Vol. 57, EAS Publications Series. EDP, pp 3–43 (arXiv:1206.1021), doi:10.1051/eas/1257001
Ammons S. M., Robinson S. E., Strader J., Laughlin G., Fischer D., Wolf A., 2006, ApJ, 638, 1004
Anderson E. R., Duvall Jr. T. L., Jefferies S. M., 1990, ApJ, 364, 699
Angulo C., et al., 1999, Nuclear Phys. A, 656, 3
Astropy Collaboration et al., 2013, A&A, 558, A33
Astropy Collaboration et al., 2018, AJ, 156, 123
Astropy Collaboration et al., 2022, ApJ, 935, 167
Baines E. K., Armstrong J. T., Schmitt H. R., Zavala R. T., Benson J. A., Hutter D. J., Tycner C., van Belle G. T., 2018, AJ, 155, 30
Ball W. H., Gizon L., 2014, A&A, 568, A123
Ball W. H., Gizon L., 2017, A&A, 600, A128
Bazot M., et al., 2011, A&A, 526, L4
Bedding T. R., et al., 2011, Nature, 471, 608
Bellinger E. P., 2022, earlbellinger/mesa-summer-school-2022: MESA Summer School 2022, doi:10.5281/zenodo.7118662, https://doi.org/10.5281/zenodo.7118662
Benson J. A., Hummel C. A., Mozurkewich D., 2003, in Traub W. A., ed., Society of Photo-Optical Instrumentation Engineers (SPIE) Conference Series Vol. 4838, Interferometry for Optical Astronomy II. pp 358–368, doi:10.1117/12.459322
Bessell M. S., 2000, PASP, 112, 961
Bessell M. S., Castelli F., Plez B., 1998, A&A, 333, 231
Blouin S., Shaffer N. R., Saumon D., Starrett C. E., 2020, ApJ, 899, 46
Böhm-Vitense E., 1958, Z. Astrophys., 46, 108
Borucki W. J., et al., 2010, Science, 327, 977
Bossini D., et al., 2015, MNRAS, 453, 2290
Bossini D., et al., 2017, MNRAS, 469, 4718
Boyajian T. S., van Belle G., von Braun K., 2014, AJ, 147, 47
Brogaard K., et al., 2023, A&A, 679, A23
Brown T. M., Gilliland R. L., Noyes R. W., Ramsey L. W., 1991, ApJ, 368, 599
Bruntt H., et al., 2010, MNRAS, 405, 1907
Campante T. L., et al., 2024, A&A, 683, L16
Cardelli J. A., Clayton G. C., Mathis J. S., 1989, ApJ, 345, 245
Cassisi S., Potekhin A. Y., Pietrinferni A., Catelan M., Salaris M., 2007, ApJ, 661, 1094
Castro-Ginard A., et al., 2024, A&A, 688, A1
Chaplin W. J., Miglio A., 2013, ARA&A, 51, 353
Chugunov A. I., Dewitt H. E., Yakovlev D. G., 2007, Phys. Rev. D, 76, 025028
Claret A., 2000, A&A, 363, 1081
Claret A., Bloemen S., 2011, A&A, 529, A75
Constantino T., Campbell S. W., Christensen-Dalsgaard J., Lattanzio J. C., Stello D., 2015, MNRAS, 452, 123
Cox J. P., Giuli R. T., 1968, Principles of stellar structure
Creevey O. L., Lebreton Y., 2022, Masses and ages from FLAME in DR3, GAIA-C8-TN-OCA-OLC-036, https://dms.cosmos.esa.int/COSMOS/doc_fetch.php?id=1612899
Cunha M. S., et al., 2007, A&ARv, 14, 217
Cunha M. S., Avelino P. P., Christensen-Dalsgaard J., Stello D., Vrard M., Jiang C., Mosser B., 2019, MNRAS, 490, 909
Cutri R. M., et al., 2003, VizieR Online Data Catalog: 2MASS All-Sky Catalog of Point Sources (Cutri+ 2003), VizieR On-line Data Catalog: II/246. Originally published in: University of Massachusetts and Infrared Processing and Analysis Center, (IPAC/California Institute of Technology) (2003)
Cyburt R. H., et al., 2010, ApJS, 189, 240
De Moura B. L., et al., 2020, ApJ, 894, 67
Deka-Szymankiewicz B., Niedzielski A., Adamczyk M., Adamów M., Nowak G., Wolszczan A., 2018, A&A, 615, A31
Derekas A., et al., 2011, Science, 332, 216
Ducati J. R., 2002, VizieR Online Data Catalog: Stellar Photometry in Johnson's 11-color system (Ducati, 2002), VizieR On-line Data Catalog: II/237. Originally published in: Departement of Astronomy, University of Wisconsin, Madison WI 53706 (2002)
Eddington A. S., 1926, The Internal Constitution of the Stars
Evans D. W., et al., 2018, A&A, 616, A4
Ferguson J. W., Alexander D. R., Allard F., Barman T., Bodnarik J. G., Hauschildt P. H., Heffner-Wong A., Tamanai A., 2005, ApJ, 623, 585
Foreman-Mackey D., Hogg D. W., Lang D., Goodman J., 2013, PASP, 125, 306
Fuller G. M., Fowler W. A., Newman M. J., 1985, ApJ, 293, 1
Gaia Collaboration 2022, VizieR Online Data Catalog: Gaia DR3 Part 1. Main source (Gaia Collaboration, 2022), VizieR On-line

[1] https://simbad.u-strasbg.fr/simbad/sim-basicIdent=m33&submit=SIMBAD+search

Data Catalog: I/355. Originally published in: doi:10.1051/0004-63, doi:10.26093/cds/vizier.1355
García R. A., Ballot J., 2019, Living Reviews in Solar Physics, 16, 4
García Saravia Ortiz de Montellano A., Hekker S., Themeßl N., 2018, MNRAS, 476, 1470
Girardi L., 1999, MNRAS, 308, 818
Girardi L., 2016, ARA&A, 54, 95
Gough D. O., 1990, in Osaki Y., Shibahashi H., eds, , Vol. 367, Progress of Seismology of the Sun and Stars. p. 283, doi:10.1007/3-540-53091-610.1007/3-540-53091-6_93
Green G. M., Schlafly E., Zucker C., Speagle J. S., Finkbeiner D., 2019, ApJ, 887, 93
Grevesse N., Sauval A. J., 1998, Space Sci. Rev., 85, 161
Grigahcène A., Dupret M.-A., Gabriel M., Garrido R., Scuflaire R., 2005, A&A, 434, 1055
Harris C. R., et al., 2020, Nature, 585, 357
Hekker S., Christensen-Dalsgaard J., 2017, A&ARv, 25, 1
Herwig F., 2000, A&A, 360, 952
Hjørringgaard J. G., Silva Aguirre V., White T. R., Huber D., Pope B. J. S., Casagrande L., Justesen A. B., Christensen-Dalsgaard J., 2017, MNRAS, 464, 3713
Huber D., 2025, arXiv e-prints, p. arXiv:2512.10002
Huber D., et al., 2011, ApJ, 743, 143
Huber D., et al., 2012, ApJ, 760, 32
Hunter J. D., 2007, Computing in Science & Engineering, 9, 90
Iglesias C. A., Rogers F. J., 1993, ApJ, 412, 752
Ireland M. J., et al., 2008, in Schöller M., Danchi W. C., Delplancke F., eds, Society of Photo-Optical Instrumentation Engineers (SPIE) Conference Series Vol. 7013, Optical and Infrared Interferometry. p. 701324, doi:10.1117/12.788386
Irwin A. W., 2012, FreeEOS: Equation of State for stellar interiors calculations, Astrophysics Source Code Library, record ascl:1211.002 (ascl:1211.002)
Itoh N., Hayashi H., Nishikawa A., Kohyama Y., 1996, ApJS, 102, 411
Jackiewicz J., 2021, Frontiers in Astronomy and Space Sciences, 7, 102
Jermyn A. S., Schwab J., Bauer E., Timmes F. X., Potekhin A. Y., 2021, ApJ, 913, 72
Jermyn A. S., et al., 2023, ApJS, 265, 15
Johnson J. A., et al., 2014, ApJ, 794, 15
Joyce M., Chaboyer B., 2018, ApJ, 856, 10
Kallinger T., et al., 2010, A&A, 509, A77
Kallinger T., et al., 2012, A&A, 541, A51
Kallinger T., et al., 2014, A&A, 570, A41
Karovicova I., White T. R., Nordlander T., Casagrande L., Ireland M., Huber D., Jofré P., 2020, A&A, 640, A25
Kass R. E., Wasserman L., 1995, Journal of the American Statistical Association, 90, 928
Kervella P., Bigot L., Gallenne A., Thévenin F., 2017, A&A, 597, A137
Kjeldsen H., Bedding T. R., 1995, A&A, 293, 87
Kjeldsen H., Bedding T. R., Christensen-Dalsgaard J., 2008, ApJ, 683, L175
Klinglesmith D. A., Sobieski S., 1970, AJ, 75, 175
Kostogryz N. M., et al., 2024, Nature Astronomy, 8, 929
Langanke K., Martínez-Pinedo G., 2000, Nuclear Phys. A, 673, 481
Li T., Bedding T. R., Huber D., Ball W. H., Stello D., Murphy S. J., Bland-Hawthorn J., 2018, MNRAS, 475, 981
Li Y., et al., 2023, MNRAS, 523, 916
Li Y., Ong J., Huber D., van Saders J., 2024, in 8th TESS/15th Kepler Asteroseismic Science Consortium Workshop. p. 24, doi:10.5281/zenodo.13689883
Li Y., et al., 2025, ApJ, 984, 125
Lightkurve Collaboration et al., 2018, Lightkurve: Kepler and TESS time series analysis in Python, Astrophysics Source Code Library (ascl:1812.013)
Lundkvist M. S., et al., 2024, ApJ, 964, 110
Maestro V., et al., 2013, MNRAS, 434, 1321
Magic Z., Collet R., Asplund M., 2013, in Alecian G., Lebreton Y., Richard O., Vauclair G., eds, EAS Publications Series Vol. 63, EAS Publications Series. EDP, pp 367–371 (arXiv:1310.4996), doi:10.1051/eas/1363041
Magic Z., Chiavassa A., Collet R., Asplund M., 2015, A&A, 573, A90
Mann A. W., Gaidos E., Ansdell M., 2013, ApJ, 779, 188
Matteuzzi M., Buldgen G., Dupret M.-A., Miglio A., Panier L., van Rossem W. E., 2025, A&A, 700, A261
Maxted P. F. L., 2023, MNRAS, 519, 3723
Mazumdar A., et al., 2009, A&A, 503, 521
Miglio A., et al., 2012, MNRAS, 419, 2077
Moravveji E., Townsend R. H. D., Aerts C., Mathis S., 2016, ApJ, 823, 130
Mosser B., et al., 2012, A&A, 540, A143
Mosser B., et al., 2014, A&A, 572, L5
Mosser B., Vrard M., Belkacem K., Deheuvels S., Goupil M. J., 2015, A&A, 584, A50
Murphy S. J., et al., 2021, MNRAS, 505, 2336
Noll A., Deheuvels S., 2023, A&A, 676, A70
Noll A., Basu S., Hekker S., 2024, A&A, 683, A189
Noll A., Basu S., Hekker S., 2025, A&A, 704, A188
North J. R., et al., 2007, MNRAS, 380, L80
Nsamba B., et al., 2021, MNRAS, 500, 54
O'Donnell J. E., 1994, ApJ, 422, 158
Oda T., Hino M., Muto K., Takahara M., Sato K., 1994, Atomic Data and Nuclear Data Tables, 56, 231
Ong J. M. J., Basu S., 2020, ApJ, 898, 127
Ong J. M. J., Gehan C., 2023, ApJ, 946, 92
Ong J. M. J., Basu S., Roxburgh I. W., 2021, ApJ, 920, 8
Ostrowski J., Baran A. S., Sanjayan S., Sahoo S. K., 2021, MNRAS, 503, 4646
Paxton B., Bildsten L., Dotter A., Herwig F., Lesaffre P., Timmes F., 2011, ApJS, 192, 3
Paxton B., et al., 2013, ApJS, 208, 4
Paxton B., et al., 2015, ApJS, 220, 15
Paxton B., et al., 2018, ApJS, 234, 34
Paxton B., et al., 2019, ApJS, 243, 10
Pérez Hernández F., García R. A., Mathur S., Santos A. R. G., Régulo C., 2019, Frontiers in Astronomy and Space Sciences, 6, 41
Piau L., Kervella P., Dib S., Hauschildt P., 2011, A&A, 526, A100
Pickles A. J., 1998, PASP, 110, 863
Potekhin A. Y., Chabrier G., 2010, Contributions to Plasma Physics, 50, 82
Poutanen J., 2017, ApJ, 835, 119
Prša A., et al., 2016, ApJS, 227, 29
Quirrenbach A., Mozurkewich D., Buscher D. F., Hummel C. A., Armstrong J. T., 1996, A&A, 312, 160
Reimers D., 1975, Memoires of the Societe Royale des Sciences de Liege, 8, 369
Ricker G. R., et al., 2015, Journal of Astronomical Telescopes, Instruments, and Systems, 1, 014003
Rogers F. J., Nayfonov A., 2002, ApJ, 576, 1064
Roxburgh I. W., 2016, arXiv e-prints, p. arXiv:1609.00568
Rudrasingam J., Bedding T. R., Pope B. J. S., Gade Pedersen M., Lund M. N., White T. R., Hey D., 2026, arXiv e-prints, p. arXiv:2602.22472
Saumon D., Chabrier G., van Horn H. M., 1995, ApJS, 99, 713
Schimak L. S., et al., 2026, arXiv e-prints, p. arXiv:2601.12773
Schwarzschild M., 1958, Structure and evolution of the stars.
Schwarzschild K., Villiger W., 1906, ApJ, 23, 284
Skrutskie M. F., et al., 2006, AJ, 131, 1163
Sobol I. M., 1967, Ussr Computational Mathematics and Mathematical Physics, 7, 86
Sreenivas K. R., Bedding T. R., Li Y., Huber D., Crawford C. L., Stello D., Yu J., 2024, MNRAS, 530, 3477
Stello D., Bruntt H., Preston H., Buzasi D., 2008, ApJ, 674, L53
Stokholm A., Nissen P. E., Silva Aguirre V., White T. R., Lund M. N., Mosumgaard J. R., Huber D., Jessen-Hansen J., 2019, MNRAS, 489, 928
Takeda Y., Tajitsu A., 2015, MNRAS, 450, 397
Tayar J., et al., 2017, ApJ, 840, 17
Tayar J., Claytor Z. R., Huber D., van Saders J., 2022, ApJ, 927, 31
Thygesen A. O., et al., 2012, A&A, 543, A160
Timmes F. X., Swesty F. D., 2000, ApJS, 126, 501
Townsend R. H. D., Teitler S. A., 2013, MNRAS, 435, 3406

Ulrich R. K., 1986, ApJ, 306, L37
VanderPlas J. T., 2018, ApJS, 236, 16
Verma K., Rørsted J. L., Serenelli A. M., Aguirre Børsen-Koch V., Winther M. L., Stokholm A., 2022, MNRAS, 515, 1492
Verma K., Maxted P. F. L., Singh A., Ludwig H.-G., Sable Y., 2024, MNRAS, 534, 3893
Virtanen P., et al., 2020, scipy/scipy: SciPy 1.6.0, doi:10.5281/zenodo.4406806
Vrard M., et al., 2015, A&A, 579, A84
Vrard M., Mosser B., Samadi R., 2016, A&A, 588, A87
Vrard M., Cunha M. S., Bossini D., Avelino P. P., Corsaro E., Mosser B., 2022, Nature Communications, 13, 7553
Wenger M., et al., 2000, A&AS, 143, 9
Wes McKinney 2010, in Stéfan van der Walt Jarrod Millman eds, Proceedings of the 9th Python in Science Conference. pp 56 – 61, doi:10.25080/Majora-92bf1922-00a
White T. R., Bedding T. R., Stello D., Christensen-Dalsgaard J., Huber D., Kjeldsen H., 2011, ApJ, 743, 161
White T. R., et al., 2013, MNRAS, 433, 1262
Zernike F., 1938, Physica, 5, 785
Zhang Q. S., 2013, ApJS, 205, 18
pandas development team T., 2020, pandas-dev/pandas: Pandas, doi:10.5281/zenodo.3509134, https://doi.org/10.5281/zenodo.3509134
ten Brummelaar T. A., et al., 2005, ApJ, 628, 453
van Belle G. T., et al., 1999, AJ, 117, 521
van Cittert P. H., 1934, Physica, 1, 201

APPENDIX A: LD-4 COEFFICIENTS

As expected, our fit does not constrain the 4 LD coefficients (a_k) of equation (3) (see Fig. A1). So, we report the reconstructed centre-to-limb intensity values of κ Cyg from its squared visibilities in Table A1.

APPENDIX B: CORNER PLOT

Since the grid-2 using exponential overshooting performs better than grid-1 for κ Cyg, we present its corresponding corner plot in Fig. B1.

This paper has been typeset from a TEX/LATEX file prepared by the author.

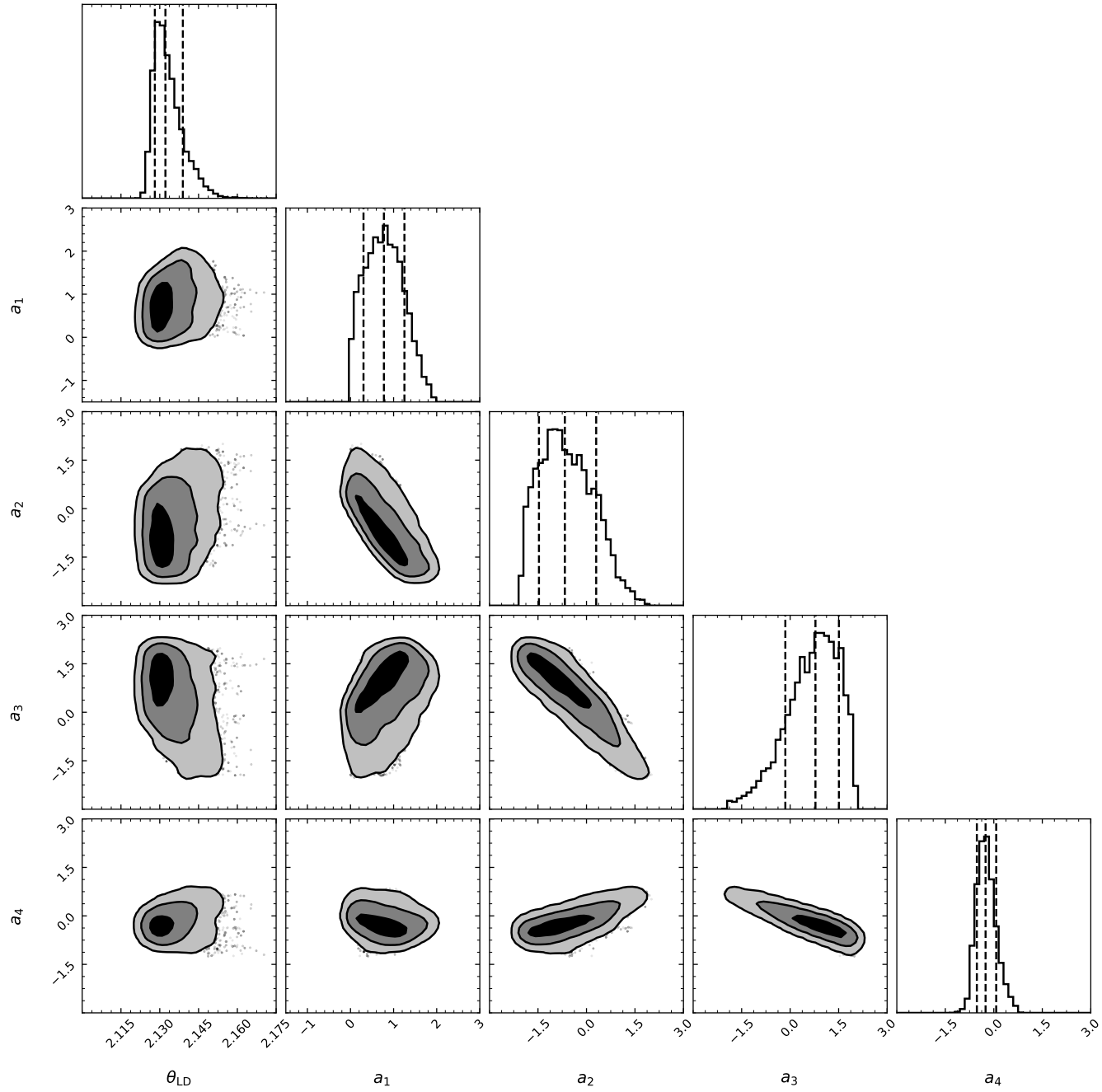

Figure A1. Corner plot of $\theta_{\rm LD}$ and LD coefficients with contour lines representing the 1, 2 and 3 σ credible regions.

μ	0.01	0.05	0.12	0.22	0.34	0.47	0.60	0.72	0.83	0.92	0.97
$\frac{I(\mu)}{I(1)}$	$0.45^{+0.08}_{-0.12}$	$0.53^{+0.05}_{-0.08}$	$0.60^{+0.03}_{-0.05}$	$0.66^{+0.02}_{-0.03}$	$0.73^{+0.01}_{-0.01}$	$0.79^{+0.00}_{-0.01}$	$0.84^{+0.00}_{-0.00}$	$0.89^{+0.00}_{-0.00}$	$0.94^{+0.00}_{-0.00}$	$0.97^{+0.00}_{-0.00}$	$0.99^{+0.00}_{-0.00}$

Table A1. Reconstructed centre-to-limb variation in intensity from direct LD fit to equation (3) for κ Cyg.

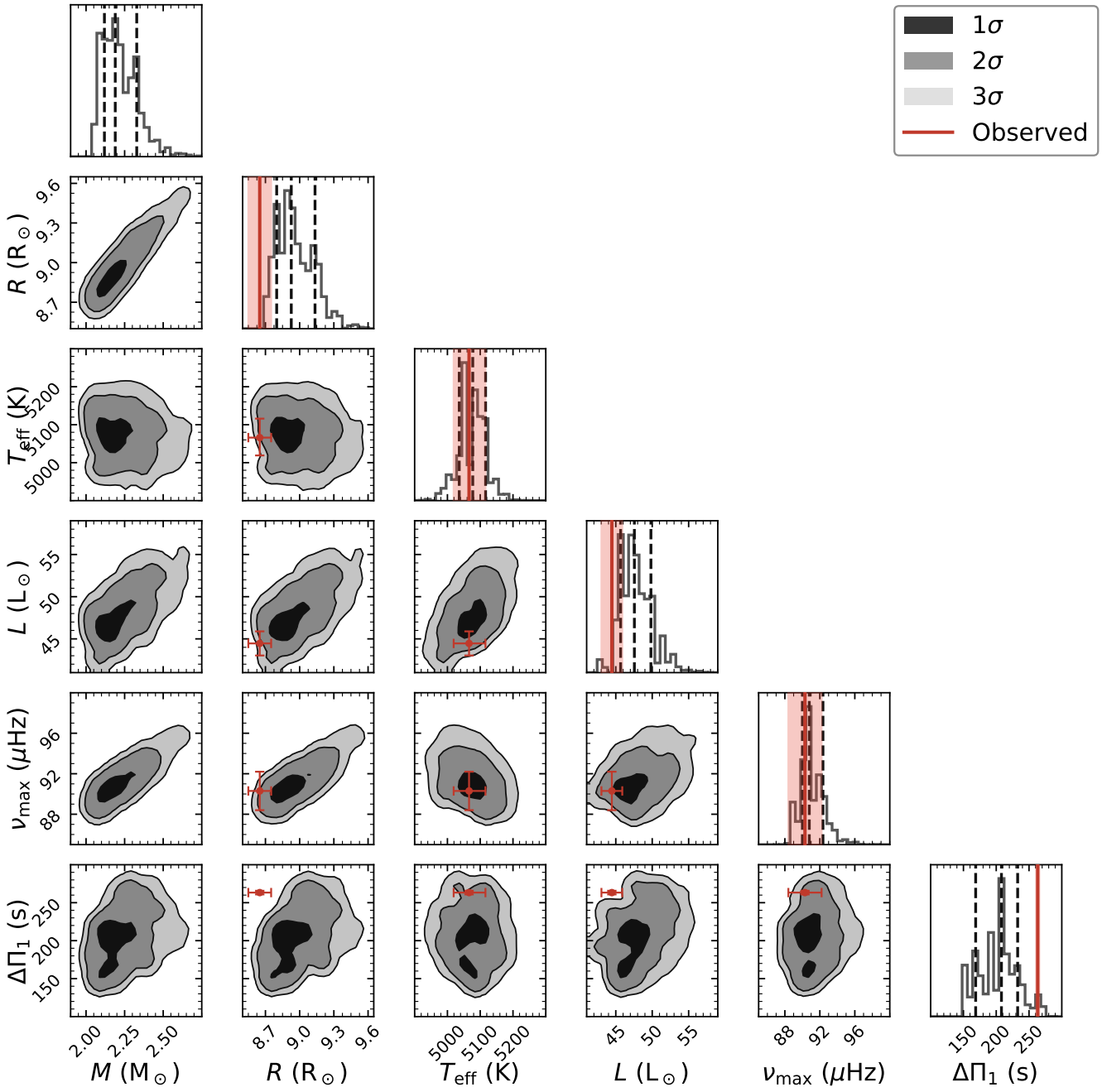

Figure B1. Corner plot for κ Cyg using grid-1 (overshooting). The grayscale panels show the normalised probability distribution calculated using a kernel density estimation (KDE). The contour lines represent the 1, 2 and 3 σ credible regions. The diagonal panels show the normalised probability distributions with the median and 1 σ quantiles shown in vertical dashed lines. The observed values are shown in red patches.